CHARLES UNIVERSITY PRAGUE

faculty of mathematics and physics

Experimental Investigation of Quantum Turbulence in Superfluid ^{4}He

Doctoral thesis

by

Tymofiy V. Chagovets

Supervisor

Prof. RNDr. Ladislav Skrbek, DrSc.

Department of Low Temperature Physics

Prague

June 11, 2008

Acknowledgements

This thesis work was carried out in the Joint Low Temperature Laboratory of the Institute of Physics and the Faculty of Mathematics and Physics UK. I am grateful to my supervisor, Professor Ladislav Skrbek, for his advises and guidance. I thank the ex–members of the group Alexey Gordeev, who performed the "counterflow" experiments discussed in this thesis and Jan Sindelar, who took part at early stages of the "pure superflow" experiment. I am also grateful to present members of our group Michaela Blažková and David Schmoranzer.

I am deeply grateful to Professor Matti Krusius, head of the Helsinki ROTA group, for providing me the opportunity for work in his laboratory. I am indebted to other members of the ROTA group, Vladimir Eltsov, Rob de Graaf and Roman Solntsev, for introducing me to ^{3}He physics and ultra low temperatures. I wish to thank our visitors A. Golov, M. Tsubota and especially W. F. Vinen for interest to our work and stimulating discussions.

I appreciate the help of Ing. František Soukup, Professor Miloš Rotter and Dr. Josef Šebek, in particular their numerous advices in electrical engineering and cryogenics. Last but not least I want to thank the technicians L. Doležal, P. Vacek and M. Zelinka for technical support and smooth supply of liquid helium.

A very special thanks go to my friends for good and memorial time. I would not have survived without the unreserved support of my family.

Finally, I would like to acknowledge the financial support of the Institutional Research Plan AVOZ10100520, GACR 202/05/0218 and GACR 202/08/0276.

Prague, 2008

Tim Chagovets

Abstract

This Thesis reports an experimental investigation of a flow of He II thermally induced by a fountain pump through vertical channels of square cross-section with ends blocked by sintered silver superleaks and its decay. We confirm the existence of a weakly temperature dependent critical velocity $v_{\rm cr}^{\rm I}$ of order 1 cm/s, which does not scale with the channel size and is therefore an intrinsic property of the self-sustained vortex tangle of vortex line density, L, measured by the second sound attenuation. In addition to the previously reported turbulent A-state characterized by $L^{1/2} = \gamma(T)(v - v_{\rm cr}^{\rm I})$ we have discovered a new B-state characterized by $L = \beta(v - v_{\rm cr}^{\rm II})$, where β seems temperature independent. It poses an important question why the quadratic generation mechanism, so well established in thermal counterflow, ceases to work. We offer a phenomenological model assuming that in the B-state the superflow matches the classical parabolic profile, with a finite, temperature dependent slip velocity $v_{\rm cr}^{\rm II}$ of order few cm/s and that a confined viscous normal fluid flow of toroidal form is induced inside the channel due to the mutual friction force. When the fountain pump is switched off, after an initial decay, a confined quasi-viscous flow of a quasi-single component fluid with effective kinematic viscosity $\nu_{eff}(T)$ establishes, giving rise to the observed exponential decay. The corresponding values of $\nu_{eff}(T)$ are calculated and presented. The Thesis also presents the temperature dependence of the effective kinematic viscosity of turbulent He II $\nu_{eff}(T)$ deduced from second sound attenuation data using the late stage of decay of thermally induced counterflow He II turbulence in two channels of square cross-section. It is shown that values of $\nu_{eff}(T)$ calculated in this Thesis agree not only with with each other, but also with the theoretical model of Vinen and Niemela and published data of $\nu_{eff}(T)$ calculated based on the Oregon experiments on the decaying grid generated He II turbulence and the recent Manchester spin down He II experiments.

Contents

Chapter 1

Introduction

. . . doue la turbolenza dellacqua sigenera
doue la turbolenza dellcq simantiene plugno
doue la turbolenza dellacqua siposa . . .

From daily experience we know that liquid can move smoothly (quietly) or the stream has properties of unpredictability and disorder. The first type of flow is called laminar, the other one turbulent. Most flows we meet in Nature are turbulent. A lot of people associate turbulence mainly with huge eddies affecting planes, but fluid turbulence is much more common phenomenon. It surrounds us every minute wherever we are. It shows, for example, in the flow of water from a common faucet and in the flow over the hull of a submarine, at moving great air masses or at mixing fuel components in a jet engine.

The first scientific document of turbulence observation is the Leonardo da Vinci's manuscript (approximately 1507 A.D.). He tried to understand the principles of liquid motion in the Arno River and named the phenomenon he observed in whirl flow *"la turbolenza"*. One of the comments which he wrote in his notes reads as follows:

"...doue la turbolenza dellacqua sigenera doue la turbolenza dellcq simantiene plugno doue la turbolenza dellacqua siposa ..."[1]

This note formulates three main questions of turbulent flows. In this Thesis, we mainly concentrate on last two problems.

Although the problem of turbulence was formulated in the beginning of 16th century, some elements of real mathematically sound turbulent theory appeared only in the end of 19th century, thanks to the famous work of Osborne Reynolds. It is based on several

[1] *"...where turbulence of water is raised where turbulence of water is kept for a long time where turbulence of water fades ..."*

Fig. 1.1: Leonardo, Old Man with Water Studies, c. 1513.

aspects of da Vinci's observations. Such unusually long empty period is connected with the complexity of solving nonlinear and multiscale problems involved in turbulent fluid flows.

There are only few basic fluid dynamical problems, such as slow flow of water in a pipe or laminar flow around various obstacles, which can be resolved analytically, based on the Navier-Stokes equation (equation of motion for a viscous fluid). Despite the fact that the Navier-Stokes equation has, in principle, a deterministic solution for a turbulent flow and can therefore be solved numerically, nonlinearity of the problem makes numerical solution hard to obtain, and for highly turbulent flows the task is in most cases impossible even for today's supercomputers.

Development of statistical physics allowed to apply another approach. Andrey Nikolaevich Kolmogorov was first who applied statistical approach to the turbulence problem, in his theory known in the turbulent community as K-41. But this is not the end of the story. Development of new parts of mathematical physics, such as fractal geometry and deterministic chaos, lead to yet another approaches to the problem of fluid turbulence.

The results obtained in frame of these approaches are frequently concerned with different aspects of the problem and answer particular questions arising in qualitatively different experimental situations. Every approach was considered to their supporters as a uniquely acceptable, so they were developed in parallel and practically independently.

Only during last 20 years or so there is a tendency to outline direction towards a uniform theory of turbulence.

This Thesis is devoted to a special branch of turbulence – quantum turbulence – taking place in quantum liquids. It is well known that liquid helium displays such an extraordinary quantum phenomenon as *superfluidity*, when a part of the fluid loses its viscosity at low enough temperature. A flow of superfluid helium differs from that of a classical viscous fluid in three important respects, all related to quantum effects: it exhibits two-fluid behavior; the superfluid component can flow without viscous dissipation; and the flow of the superfluid component is subject to severe quantum restrictions.

There are two stable isotopes of helium: ^{3}He and ^{4}He. Superfluid ^{3}He exists in several superfluid phases with numerous types of topological defects. It represents an extremely pure system which allows, for example, to create a single quantized vortex and to investigate its dynamics or multiplication. But such type of experiment needs a complicated technique connected with achieving of ultra low temperature of order 1 mK.

Other possibility is to investigate quantum turbulence in superfluid ^{4}He, where we do not need such a low temperature and an extremely sensitive experimental tool - second sound attenuation - can be used. The existence of a "virgin" sample, i.e., without any quantized vortex line is hardly possible here, as any solid wall ought to be considered as rough on the scale of the size of the vortex core, and, consequently, remnant vortex lines are always present in any macroscopic sample of superfluid ^{4}He. On the other hand, there are many experiments with superfluid ^{4}He where quantum turbulence can be created by various thermal or mechanical means, which, we believe, ought to provide with valuable experimental data leading to better understanding of the phenomenon of fluid turbulence in general. This is main motivation for the work reported in this Thesis devoted to experimental investigation of thermally induced quantum turbulence in He II.

Chapter 2

Theoretical Background

The thorough and long-lasting investigation of physical properties of liquid helium begun since helium was first liquefied by Heike Kamerlingh Onnes in 1908. During those 100 years, many researchers worked on various aspects of behavior of this extraordinary liquid. In particular, turbulence in helium – the topic of this Thesis – has been an object of study for more than half a Century. The aim of the Theoretical background is to describe those properties, which, according to my mind, are important for understanding of our experiments.

2.1 Selected Physical Properties of He II

Below $T_\lambda = 2.172$ K liquid ^{4}He becomes superfluid and is referred to as He II – a quantum fluid that exhibits extraordinary flow properties [1, 2, 3]. They can largely be understood within a phenomenological two fluid model, where, in the limit of low flow velocities, He II is described as consisting of two interpenetrating fluids of independent velocity fields. One is the inviscid superfluid of density ρ_s, the other one the normal fluid of density ρ_n and dynamic viscosity η; the total density is therefore

$$\rho = \rho_s + \rho_n \,. \tag{2.1}$$

The mass flux of fluid $\vec{j}$ is given by

$$\vec{j} = \rho_s \vec{v_s} + \rho_n \vec{v_n} \,. \tag{2.2}$$

The total mass is conserved, thus we can write the continuity equation in the form

$$\frac{\partial \rho}{\partial t} = -\vec{\nabla} \cdot \vec{j} \,. \tag{2.3}$$

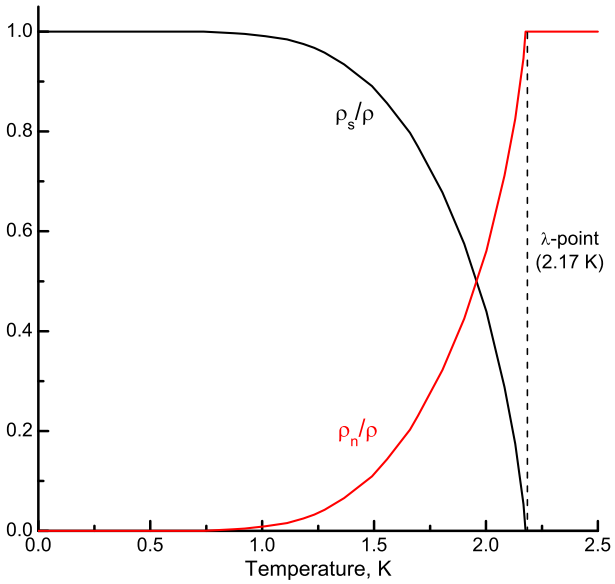

Fig. 2.1: The normal and superfluid density ratios vs temperature.

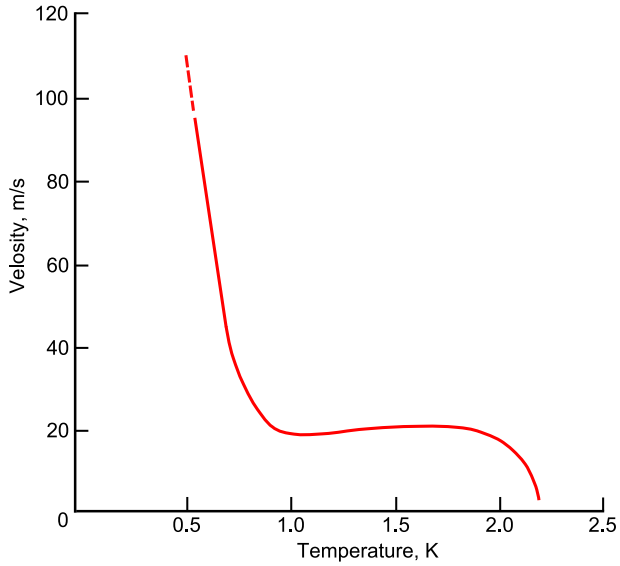

Fig. 2.2: Temperature dependence of the second sound velocity.

The normal and superfluid density ratios (see Fig. 2.1) were first measured in the famous Andronikashvili experiment [2]. The superfluid has neither viscosity nor entropy, thus the entire heat content of He II is carried by the normal component. This simplified picture is reflected by the Landau two-fluid model [3].

In order to avoid unnecessary complexity, we first consider the limit of low flow velocities: the superfluid velocity v_s is much smaller than that at which dissipation takes place; and the velocity of the normal component v_n is much smaller than the value at which turbulence appears. According to Landau, the equations of motion for the superfluid and for the normal fluid can be written as

$$\rho_s \left\{ \frac{\partial \vec{v}_s}{\partial t} + (\vec{v}_s \cdot \nabla)\vec{v}_s \right\} = -\frac{\rho_s}{\rho}\nabla p + \rho_s \sigma \nabla T \ , \tag{2.4}$$

$$\rho_n \left\{ \frac{\partial \vec{v}_n}{\partial t} + (\vec{v}_n \cdot \nabla)\vec{v}_n \right\} = -\frac{\rho_n}{\rho}\nabla p - \rho_s \sigma \nabla T + \eta_n \nabla^2 \vec{v}_n \ . \tag{2.5}$$

These equations are of Euler and Navier-Stokes type, but with the addition of thermal gradient terms. These equations are valid as soon as v_s and v_n are sufficiently small. One important outcome of these equations is the prediction of second sound – a wave described by temperature fluctuations rather than by density fluctuations as is the case of the ordinary sound, also referred to as first sound. Expressions for the first and second sound velocities derived from the equation of the continuity (Eq. 2.3) and from the two-

fluid equation (Eq. 2.4 and 2.5) read:

$$u_1^2 = \left(\frac{\partial p}{\partial \rho}\right)_\sigma , \tag{2.6}$$

$$u_2^2 = \frac{\rho_s}{\rho_n}\sigma^2 \left(\frac{\partial T}{\partial \sigma}\right)_p , \tag{2.7}$$

where p is the pressure and σ is the entropy per unit mass. The dependence of second sound velocity on temperature is presented in Fig. 2.2. The second sound can be considered as an antiphase motion of the two fluids, thus total flow of matter at every moment stays constant. Standing waves of second sound can be generated by a suitable transmitter (e.g., in a form of an electrical heater) and detected, e.g., by a resistance thermometer. Other possibility is to use a pair of porous membranes fixed opposite each other. The transducer membrane is oscillating and pushing the normal component (which, due to finite viscosity, cannot penetrate through the pores), while the inviscid superfluid penetrates freely. This leads to antiphase motion of the two fluids and, as a result, second sound waves become generated. This method will be discussed in detail in Chapter 3.1.1

2.2 Quantum mechanical description of He II

From the quantum mechanical point of view an ansamble of ^{4}He atoms is governed by the Bose-Einstein statistics, as spin of the ^{4}He atom is zero. It is well known that in the low temperature limit a macroscopic number of particles of an ideal Bose–gas occupy the same quantum state on the lowest energy level. This phenomenon occurring in the 3D momentum space is known as Bose–Einstein condensation. Let us assume that liquid ^{4}He below the λ–point contains condensate. In steady state it can be described by the macroscopic wave function:

$$\Psi(r) = \Psi_0 exp[iS(r)] , \tag{2.8}$$

where Ψ_0 is its amplitude and $S(r)$ is the macroscopic phase. The canonical momentum of the condensate can be expressed as:

$$\vec{p} = \hbar \nabla S .$$

It can be interpreted as the momentum per one particle of the superfluid with the superfluid velocity

$$\vec{v}_s = \frac{\hbar}{m_4} \nabla S ,$$

where m_4 is the mass of ^{4}He. As one can see, the superfluid velocity is proportional to the gradient of the phase. It follows that the $curl$ of superfluid velocity:

$$curl\ \vec{v}_s = 0\ . \tag{2.9}$$

These hydrodynamic properties of He II clearly demonstrate that superfluidity can be interpreted as quantum mechanical behavior on macroscopic scale.

2.3 Quantized vortices in He II and their detection

Equation 2.9 corresponds to the condition with no quantized vortices in the superfluid. However, it is possible to prove that circulation in a multiply connected region[1], defined as

$$\chi = \oint \vec{v}_s d\vec{l} = \frac{\hbar}{m_4} \oint \nabla S d\vec{l}$$

is quantised. The phase can be zero or plus/minus any integer times 2π, while the value of the superfluid macroscopic wave function remains single-valued. Thus the quantization condition for circulation yields

$$\chi = n\frac{\hbar}{m_4} = \pm n\kappa\ ,$$

where $\hbar$ is the Planck constant, n = 0, 1, 2, ... and

$$\kappa = \frac{\hbar}{m_4}\ . \tag{2.10}$$

The quantity κ is known as the quantum of circulation and in ^{4}He equals to 9.997×10^{-8} m^2/s.

The core of the vortex of size of order the healing length $\xi \approx 0.1$ nm does not contain superfluid component and inside it $curl\ \vec{v}_s \neq 0$. A series of concentric circular streamlines are surrounding the vortex core. Superfluid velocity decreases from the vortex axis as $v_s \propto r^{-1}$, where r is the distance from the axis.

The presence of vortices in He II leads to interaction between the normal fluid and the superfluid known as the *mutual friction* force [4, 5]. The microscopic origin of the mutual friction force is scattering of the normal fluid made up by the elementary excitations – photons and rotons – off the vortex core. Let us mention in passing that the first unequivocal proof of existence of quantized vortices and of the magnitude of their circulation quantum was obtained indirectly, using the vibrating wire technique, by Vinen [6].

[1] An example of multiply connection region is the space between two coaxial cylinders filled with He II.

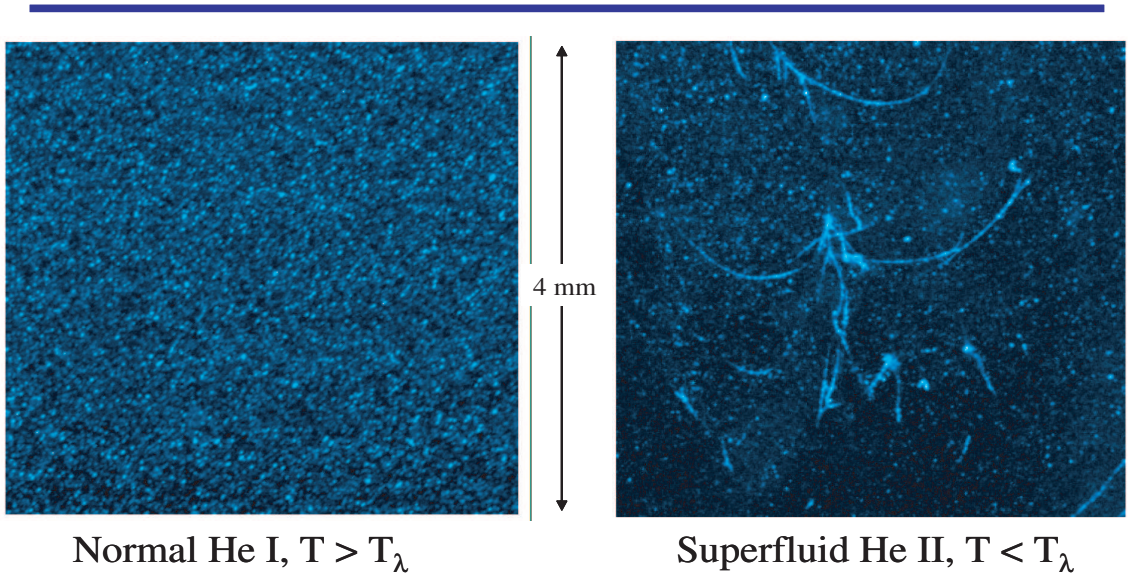

Fig. 2.3: The photograph of small hydrogen-deuterium "snowballs" in normal liquid He I (left) and in superfluid He II, where they are attracted by the Magnus force to the cores of quantized vortices and decorate them. Quantized vortices appear spontaneously when the liquid is cooled through the superfluid transition.

The most direct approach to prove the existence of quantized vortices is straight visualization of them, using the sophisticated technique of particle image velocimetry (PIV), where as working particles small hydrogen-deuterium "snowballs" can be used. This approach, however, proved difficult to realize and it is only very recently that successful results such as shown in Fig. 2.3 have been obtained [7].

There are several other methods how one can detect quantized vortices. Both positive and negative [8] ions can serve as probes to detect them, and indeed the ion method was first to take photographs of the geometry of the vortex lattice appearing in the rotating bucket [9].

In this Thesis, we concentrate on detection of quantized vortices in He II using so called *second sound attenuation technique*. Second sound technique was used since the very beginning of this research, starting with pioneering experiments of Hall and Vinen with rotating containers of He II [4, 5]. It was later discovered that, at constant angular velocity, the basic state of rotation of the superfluid component of He II is represented by regular configuration of vortex lines, which are parallel to the axis of rotation. In the experiment, when second sound waves were propagating in the direction along vortex lines, no perceptible excess attenuation of second sound was detected. On the other hand, it was shown that the excess attenuation of second sound, α_L, propagating in the direction

perpendicular to the rotation axis, due to the presence of quantized vortices becomes

$$\alpha_L = \frac{B\Omega}{2u_2} \, , \tag{2.11}$$

where Ω is the angular velocity of the container, u_2 is the second sound velocity and B is a phenomenological parameter described below. Later Eq. 2.11 was derived phenomenologically by Bekarevich and Khalatnikov [10]. This extra attenuation results from the scattering of the elementary excitations, which make up the normal fluid, by vortex lines.

Let us discuss the case of rotating bucket of He II in some more detail. In solid body rotation the vorticity of the normal viscous fluid ω_n ought to be written in a usual way, as

$$\vec{\omega}_n = 2\vec{\Omega} \tag{2.12}$$

Since the superfluid mimics solid body rotation by creation of a lattice of rectilinear quantized vortices aligned in the direction of the rotation axis, the vorticity ω_s, on average, is given by

$$\langle \omega_s \rangle = 2\Omega = \kappa L \, , \tag{2.13}$$

where the quantity L, called vortex line density, is the total length of the vortex line per unit volume.

Let us consider a simple rotating one-dimensional second sound resonator (second sound propagating normally to the rotation axis), where the second sound resonance can be considered as an infinite series of reflected second sound waves. The extra attenuation, [11] due to rectilinear quantized vortices that are created during rotation, becomes

$$\alpha_L = \frac{B\kappa L}{4u_2} = \frac{\pi\Delta_0}{u_2}\left(\frac{a_0}{a} - 1\right) \, , \tag{2.14}$$

where a and a_0 are the amplitudes of the second sound standing wave resonance with and without vortices present, respectively.

If second sound propagates at arbitrary angle with respect to the direction of vortex lines, the phenomenological mutual friction parameter B have to be replaced in Eq. 2.11 by $Bsin^2(\Theta) + B''cos^2(\Theta)$, where Θ is the angle between the direction of the quantized vorticity and the direction of second sound propagation. The second term, containing another (nondissipative) phenomenological mutual friction parameter B'' is small and except very close to the lambda temperature can be neglected, resulting in

$$\alpha_L = \frac{Bsin^2(\Theta)\Omega}{2u_2} \tag{2.15}$$

This so-called "sine squared law" has been confirmed experimentally by measuring second sound signals in a container filled with superfluid helium held at tilted angles with

respect to the axis of the rotation cryostat [12, 13]. We shall describe later how the second sound detection technique can be used in investigations of quantum turbulence in He II.

2.4 Quantum Turbulence

Turbulence in the superfluid component of ^{4}He was first mentioned as a theoretical possibility by Feynman [14], who suggested that it takes the form of a random tangle of quantized vortex lines. Quantum turbulence, a form of turbulence observed in superfluids, differs from that in classical fluids for three reasons: except at the lowest temperatures, superfluids exhibit two-fluid behaviour; the superfluid component can flow without dissipation; and superflow is subject to severe quantum restrictions, so that rotational motion can exist only through the presence of quantized vortex lines. In spite of these differences there is evidence that quantum turbulence can exhibit features similar to those observed in its classical counterpart, especially on large length scales.

Quantum turbulence can be probably most generally defined as a way of motion of a quantum fluid that involves dynamics of a tangle of quantized vortices. It can exist in various quantum fluids - besides He II in superfluid phases of ^{3}He, in ^{3}He - ^{4}He mixtures, in Bose-condensates of alkali atoms or perhaps even in neutron stars. Experimental investigations have been so far restricted to He II and the fermionic superfluid ^{3}He-B. As atoms of ^{3}He are fermions and Cooper pairs of ^{3}He atoms have spin $S = 1$, nuclear magnetic resonance technique therefore serves as a powerful tool of its investigation and quantum turbulence in ^{3}He can be detected and investigated by an NMR spectrometer [15]. Additionally, thanks again to the fermionic nature of superfluid ^{3}He-B, quantum turbulence can be probed by vibrating wires [16] or piezoelectric quartz tuning forks [17] using so called Andreev scattering technique. Although the author of this Thesis spent three months visiting Low Temperature Laboratory, Helsinki University of Technology in Finland and actively participated in experimental ^{3}He-B quantum turbulence research, considerations of quantum turbulence in superfluid phases of ^{3}He lays beyond the scope of this Thesis. Leaving aside also other exotic possibilities of quantum turbulence mentioned above, unless especially mentioned, by quantum turbulence we shall mean turbulence in the superfluid phase of the common isotope of helium, ^{4}He.

Turbulence in He II can be created *classically*, i.e., in a same way as it is usually done in classical viscous fluids. Examples are an impulsive spin-down of a rotating bucket [8], or towing a grid of bars through a stationary sample of He II in a channel [18, 11, 19]. These types of turbulence in He II are in many ways analogous with the classical turbulence in

an ordinary viscous liquid.

Another possibility is to create He II turbulence thermally, which, due to the two-fluid behavior, has no direct classical analog in conventional hydrodynamics. The prime examples are thermal counterflow [20, 21, 22] and pure superflow in a flow channel [23, 24, 25]. In this Thesis, we shall mainly consider He II turbulence which is thermally driven.

2.4.1 Thermal counterflow in He II

The two fluid equations 2.4 and 2.5 explain the existence of a peculiar flow of He II called counterflow – under influence of applied heat the superfluid moves to the heat source, becomes converted into the normal fluid which flows against the approaching superfluid in such a way that the total density of He II stays unchanged [1, 2].

Thermal counterflow can be easily set up by applying a voltage to a resistor (heater) located at the closed end of a channel open to the helium bath at the other end. The heat flux is carried away from the heater by the normal fluid alone, and, by conservation of mass, a superfluid current arises in the opposite direction. In this way a relative (counterflow) velocity $\vec{v}_{ns} = \vec{v}_n - \vec{v}_s$ is created along the channel which is proportional to the applied heat flux, $\dot{q} = \dot{Q}/A$, where A is the cross–section of the flow channel, which for simplicity we assume constant. Assuming that the power $\dot{Q}$ applied at the heater is used to convert superfluid into normal fluid, the velocity of the outgoing normal fluid is $v_n = \dot{q}/(ST\rho)$, where S is the specific entropy of He II. The counterflow velocity v_{ns} is then easily established from the condition $\rho_s v_s + \rho_n v_n = 0$.

This simple physical picture holds only at low counterflow velocities. Already at relatively small values of v_{ns} of order 1 cm/s the flow and the heat transfer becomes affected by quantum turbulence – due to the appearance of an apparently disordered tangle of superfluid vortex lines. Its intensity is represented by the vortex line density L - total length of vortex lines in a unit volume. The steady state counterflow He II turbulence and its decay has been a subject of investigation by many authors [20, 21, 22]. A phenomenological model for description of vortex dynamics based on the concept of a random vortex tangle of line density L was introduced by Vinen [20, 26] and backed up by Schwarz [27] using rather general arguments tracing back to the equation of vortex motion in local approximation. The phenomenological Vinen equation (its slightly simplified form, but adequate for our purpose here) reads:

$$\frac{\partial L}{\partial t} = \frac{\rho_n B}{2\rho}\chi_1 v_{ns} L^{3/2} - \frac{\kappa}{2\pi}\chi_2 L^2 \,, \tag{2.16}$$

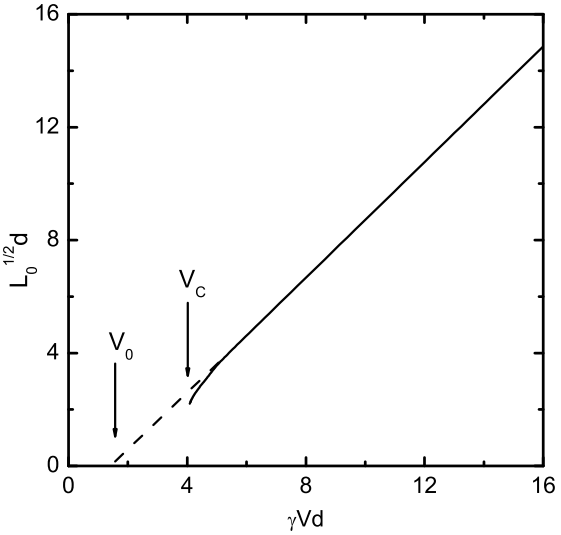

Fig. 2.4: The square-root of the vortex line density L_0 versus the relative velocity V (see Eq. 2.17) plotted in dimensionless form.

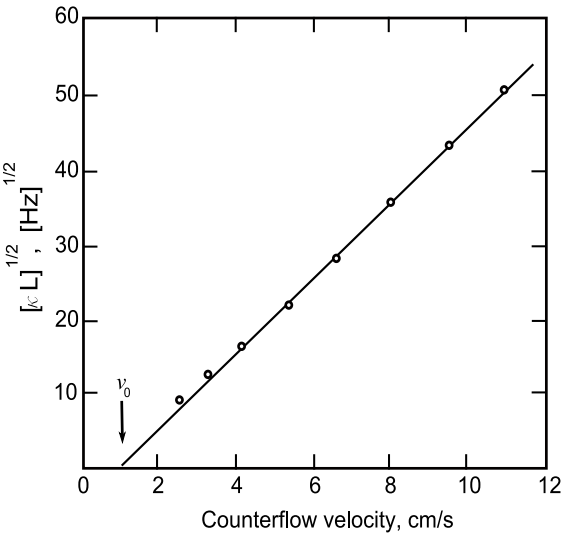

Fig. 2.5: The square-root of the vortex line density as a function of counterflow velocity at 1.7 K.

where v_{ns} is the counterflow velocity, χ_1 and χ_2 are undetermined dimensionless constants and B is the temperature dependent (and weakly frequency dependent) mutual friction coefficient, tabulated in [28]. The first term on the right hand side (RHS) describes production of the turbulence; the last term on the RHS its decay. The steady state solution of the Eq. 2.16 obtained by setting $\partial L/\partial t$ to zero is

$$L_0 = \gamma^2 v_{ns}^2 \,, \tag{2.17}$$

where

$$\gamma = \frac{\pi B \rho_n \chi_1}{\rho \kappa \chi_2} \,. \tag{2.18}$$

Thus the vortex line density is proportional to the square of the counterflow velocity, and the steady state value determines the ratio of the phenomenological constants χ_1 and χ_2.

The principle Vinen' result based on the second sound steady state measurements in a wide channel is shown in Fig. 2.4. This experiment demonstrated that the mutual friction force is zero below some critical velocity and increases when the flow velocity exceeds it. Thus below the critical velocity the flow of the superfluid component is potential and the flow of the normal component is always laminar. Dissipation is provided by the normal fluid viscosity only. This result was later confirmed also in our laboratory in experiments on steady-state and decaying counterflow (see Fig. 2.5).

Following the Vinen' pioneering experiments [20, 26], the counterflow turbulence was subsequently experimentally investigated by many authors [21, 20, 26, 29, 30, 31]. Tough with co-authors investigated thermally induced counterflow turbulence in the channel of small cross-section [21]. Measuring the temperature difference between the ends of the flow tube, his group discovered two turbulent states denoted as T I and T II. Above some second critical counterflow velocity the behavior of vortex line density changes. The T I state agrees with the homogeneous theory of Schwarz [27] only qualitatively while for the T II state this theory works rather well. It was claimed by Tough that the T I state might not be homogeneous and isotropic.

2.4.2 Pure superflow in He II

Tough and coworkers investigated pure superflow with the same flow tube. Their method uses a superleak, which in a clever way prevents the normal fluid flow through the tube. The term pure superflow thus means the net flow of the superfluid component trough the pipe only. Surprisingly, only one turbulent state [24] was found, as opposed to the two in thermal counterflow. The result of both complementary experiments presented in term of vortex line density is shown in Fig. 2.6.

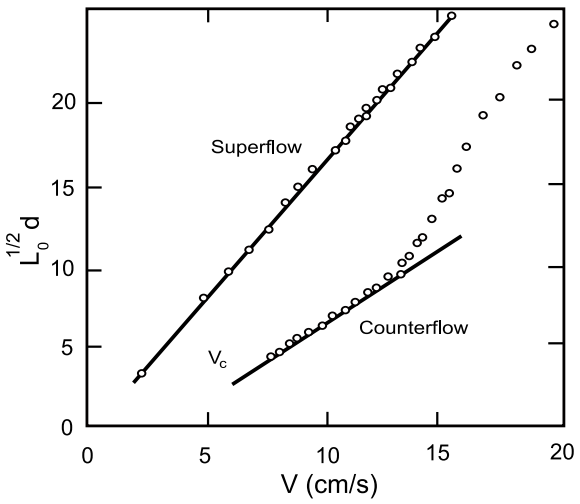

Fig. 2.6: The vortex line density (in dimensionless form) for thermal counterflow and pure superflow as a function of the relative velocity.

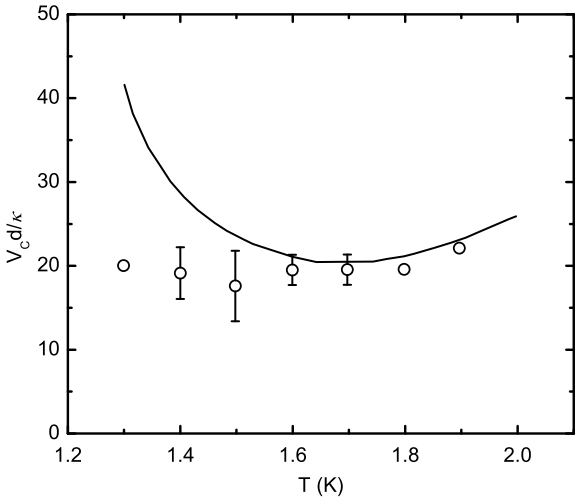

Fig. 2.7: The dimensionless critical superfluid velocity measured at various temperatures. The temperature dependence determined by the Schwarz model is shown by the solid line.

The physical properties of pure superflow can be described by vortex line density L

of the form given by Eq. 2.17. The early experimental observations of pure superflow both in cylindrical ($id = 0.13$ mm) and rectangular (0.057×0.057 mm^2) cross–section channels did not display any evidence of critical velocity [23, 32, 25]. Only later careful experiments in a circular (id = 0.13 mm) tube confirmed the finite nearly temperature independent value v_{cr}^I, of about 1.5 cm/s [33], which was defined as the minimum velocity at which any dissipation was observed. Figure 2.7 shows temperature dependence of critical velocity obtained from Tough's experiments and Schwarz numerical calculations in a dimensionless form of "superfluid Reynolds number" $Re_s = v_{cr}^I d/\kappa$. The dimensionless form was chosen because it was assumed, in analogy with experimental results on thermal counterflow, that the critical velocity scales with the size of the channel, d.

2.4.3 Detection of Quantum turbulence in He II Using Second Sound

We have shown above how the second sound attenuation can be used to detect the array of quantized vortices, depending on the angle between the second sound propagation and the direction of the detected quantized vorticity, leading to the "sine squared" law [12, 13]. Let us generalize this method for detection of quantum turbulence., following the work [34, 35]

Let us consider a strictly homogeneous quantum turbulence of vortex line density L in a channel. The generated second sound wave propagates across this rectangular channel of finite dimension, normally to the axis and the channel, which acts therefore as a one-dimensional second sound resonator. In view of forthcoming discussion of our results, it is useful to consider two limiting cases: (i) the tangle is fully isotropic; (ii) the tangle is polarized in such a way that all quantized vortices lie in planes perpendicular to the vector of the mean velocity flow, coincident with the axis of the channel. We shall later show that the latter case is possible when He II flows through a channel, it has a velocity flow profile which leads to a (partial) polarization of quantized vortex lines in such planes. Assuming now that *all* vortices lie in planes perpendicular to the direction of the flow, we have to take the average of $sin^2(\Theta)$ over the unit disc:

$$\left\langle sin^2(\Theta) \right\rangle = \frac{1}{2} \, ;$$

where $\langle \ \rangle$ denotes the average over the unit disc. The second sound sensor therefore detects:

$$L_{eff} = \frac{L}{2} \, .$$

In the former case, when vortex lines is assumed fully isotropic, we have to average over

the unit sphere:

$$\left\langle sin^2(\Theta)\right\rangle = \frac{2}{3}\ ;$$

here $\langle\ \rangle$ denotes the average over the unit sphere and the sensor will detect:

$$L_{eff} = \frac{2L}{3}\ .$$

Thus when the vortex tangle is considered as homogeneous and isotropic, taking into account the "sine squared: law, Eq. 2.14, ought to be rewritten as:

$$L = \frac{6\pi\Delta_0}{B\kappa}\left(\frac{a_0}{a} - 1\right)\ . \tag{2.19}$$

We shall use this expression when deducing the vortex line density from our second sound data. It is easy to write the corresponding formula for the vortex line density for the fully polarized tangle.

It follows from this analysis that when the degree of polarization of the vortex tangle is not known, this method provides information on the vortex line density with the relative accuracy up to about 1/8; moreover, when the degree of polarization of the tangle changes (e.g., during the decay of turbulence), the method would spuriously indicate it as a change in the vortex line density.

2.5 Classical Turbulence

We have already mentioned that under some circumstances turbulence in He II displays features similar to those of classical turbulence in viscous fluids. It is useful therefore to remind some of its main features. A particularly simple but important form of classical turbulence is produced by steady flow through a grid.

2.5.1 Classical Grid Turbulence

At a significant distance downstream from the grid the turbulence is at least approximately homogeneous and isotropic (HIT), and the development of an understanding of this simple form of turbulence has been important in contributing to our general understanding of turbulent flow [36, 37]. Jets of fluid emerging from the grid are unstable and break up into turbulent eddies of various sizes. The turbulent wakes formed behind each element of the grid merge at a distance from the grid much greater than the mesh of the grid, M. Eddies of various sizes are coupled and turbulent energy flows without dissipation (as long as the Reynolds number is large) from the large scale eddies (size D) into

smaller eddies (size d). This process, known as Richardson cascade, continues until small eddies with Reynolds numbers of order unity dissipate the turbulent energy by viscosity. The range of length scales over which there is negligible dissipation is called the *inertial range*.

The important statistical property of HIT is the energy spectrum, $E(k)$, such that the average turbulent energy per unit mass in the range of wavenumbers dk is $E(k)dk$. Inside the fully developed cascade $2\pi/D \ll k \ll 2\pi/d$ that is in the inertial range, the spectrum can depend on only k and the energy decay rate $\varepsilon = -dE/dt$. It follows from a dimensional argument that $E(k)$ must have the Kolmogorov form

$$E(k) = C\varepsilon^{2/3}k^{-5/3}\,, \tag{2.20}$$

where C is a dimensionless quantity known as the Kolmogorov constant. In fully-developed turbulence most of the energy is concentrated in the largest (energy containing) eddies. Examination of the form of the Navier-Stokes equation shows that the non-linear coupling will cause a transfer of energy from these energy-containing eddies in a time of order D/U (the turnover time), where U be the characteristic velocity associated with these eddies. Thus the rate at which the energy containing eddies lose energy per unit mass $\varepsilon \approx U^3/D$. This energy is being dissipated at large wavenumbers by viscosity, and this dissipation rate can be shown to be

$$\varepsilon = -\frac{dE}{dt} = \nu\omega^2 \tag{2.21}$$

where ν stands for the kinematic viscosity and $\vec{\omega} = curl\ \vec{v}$ is the vorticity in the flow.

So far our considerations on classical turbulence assumed its steady-state. However, one of cornerstones in investigation of turbulence is understanding how does it decay. The investigation of decaying turbulence is indeed an interesting and still partly open problem of fluid dynamics. Studies of the decay can help to understand the nature of the phenomenon of fluid turbulence in general. It is not our aim to describe all the complexity of decaying classical turbulence; we shall focus on one particular model that later will become relevant to our experiments on decaying quantum turbulence.

2.5.2 Classical Spectral Decay Model

Let us introduce a simplified version (for full version, see [38]) of a classical spectral decay model of decaying HIT. It assumes that at early times we have a generally accepted form

of the 3D energy spectrum

$$E(k) = 0 \ ; \ k < 2\pi/D \tag{2.22}$$

$$E(k) = Ak^m \ ; \ m = 2 \ ; \ 2\pi/D \leq k_1(t) \tag{2.23}$$

$$E(k) = C\varepsilon^{2/3}k^{-5/3} \ ; \ k_2(t) \leq k \leq \gamma(\varepsilon/\nu^3)^{1/4} = 2\pi\eta_{eff} \tag{2.24}$$

$$E(k) = 0 \ ; \ k > \eta_{eff} \tag{2.25}$$

which reflects the fact that eddies larger than the size of the turbulence box cannot exist. The high wave number exponential tail is approximated by a sharp cutoff at the effective Kolmogorov dissipation scale η_{eff} by introducing the dimensionless factor γ of order unity. In the vicinity of the energy containing length scale $\ell_e = 2\pi/k_e(t)$, where $k_1(t) < k_e(t) < k_2(t)$, the spectral energy density displays a broad maximum whose shape does not have to be exactly specified. Evaluating the total turbulent energy by integrating the 3D spectrum over all k leads to a differential equation for decaying turbulent energy and applying $\varepsilon = \nu\omega^2$ leads to a differential equation for decaying vorticity, the quantity we are primarily interested here.

At the early decay the spectrum stays self-similar. For $D \gg \ell_e \gg \eta_{eff}$ the decay is

$$E(t + t_{vo1}) = E(\tau) \propto \tau^{-2\frac{m+1}{m+3}} \ ; \ \ell_e \propto \tau^{\frac{2}{m+3}} \ ; \ \omega \propto \tau^{\frac{3m+5}{2m+6}} \ . \tag{2.26}$$

Here t_{vo1} is the virtual origin time, when the decaying turbulent energy would have been infinitely large. Assuming validity of the Saffman invariant $(m = 2)$, we obtain the **first regime** for decaying vorticity, $\omega \propto \tau^{-11/10}$.

As the turbulence decays further and $\ell_e \propto \tau^{2/5}$ grows, the lowest physically significant wave number becomes closer to the broad maximum around $2\pi/\ell_e$. The low wave number part of the spectrum can no longer be approximated as Ak^m with $m = 2$. Instead, it can be characterized by an effective power that decreases as the turbulence decays, such that $0 < m < 2$. Formula 2.26 then shows that the decay rate slows down. As ℓ_e approaches D, m becomes effectively zero and we arrive at the **second regime** of the decay $\omega \propto \tau^{-5/6}$.

At the saturation time, t_{sat}, the vorticity reaches its saturation value, ω_{sat}, and the growth of ℓ_e is completed. Still neglecting the cutoff of the spectrum at η_{eff}, the **universal third regime** is predicted as

$$\omega(t + t_{vo2}) = \omega(\tau) = \frac{\sqrt{27}D}{2\pi}\sqrt{\frac{C^3}{\nu}}\tau^{-3/2} \tag{2.27}$$

with the different virtual origin time t_{vo2}. This regime is universal in that no matter what the starting level of turbulence was (providing it was high enough to neglect viscosity corrections), the decaying system must sooner or later reach it.

So far we neglected a role of the high wave number cutoff of the energy spectrum at η_{eff}. As the vorticity decays and the Kolmogorov scale grows, the relative importance of this cutoff increases and a simple power cannot any longer describe the decay of vorticity. It was shown by [18] that after saturation of the energy containing length scale by the size of the turbulence box the decay of vorticity is more accurately described as

$$\omega(\tau) = \frac{3\nu}{2^3\gamma}\frac{2\pi}{D}^2\frac{t_B}{\tau}^{3/2} cos^3\theta \quad , \tag{2.28}$$

where

$$cos^2(3\theta) = \tau/\tau_B \tag{2.29}$$

and

$$\tau_B = \frac{16C\gamma^{4/3}}{9\nu}\frac{2\pi}{D}^2 \ . \tag{2.30}$$

Naturally, for $\gamma \to \infty$ expression 2.28 reduces to the simple power law 2.27. Formally, as the vorticity decays, η_{eff} becomes the size of the turbulent box D and both the turbulent energy and vorticity vanish. Close to this stage, however, applicability of the spectral decay model is no longer justified.

This decay model has been successfully applied to a number of wind tunnel experiments as well as to the decaying turbulence generated in water by an oscillating grid by [39], where the effect of saturation the energy containing length scale is clearly seen. Moreover, the validity of the model was confirmed by computer simulations of decaying turbulence in a bounded domain [40].

2.5.3 Classically Generated He II Turbulence and its Decay

Interest in quantum turbulence greatly grew in the nineties of the last century, in view of experiments where He II turbulence was generated classically. It was soon realized that thanks to coupling of large normal and superfluid eddies by the mutual friction force, classical and quantum turbulence (despite severe quantum-mechanical restrictions for superflow outlined above) bear important similar features and that quantum turbulence may help in deeper understanding of fluid turbulence in general.

Let us mention two experiments showing that classically generated He II turbulence is very similar in its characteristics to classical turbulence in viscous fluids, despite the two-fluid behavior of He II and quantization of circulation in its superfluid component. The first one is the experiment of Maurer and Tabeling [41], which investigates turbulence created between two counterrotating discs. In this experiment, fluctuations of the pressure head in both He I and He II steady-state turbulence were monitored by a small

sensitive pressure sensor, allowing evaluation of the frequency power spectra. Both in He I and He II the results strongly suggest the existence of the three-dimensional energy spectra containing an inertial range of scales of the classical Kolmogorov form $C\varepsilon^{2/3}k^{-5/3}$, where k denotes the wave number and $\varepsilon = -dE/dt$ is the energy decay rate. Moreover, from measurements of the skewness factor of the velocity increments, the authors found the value of the 3D Kolmogorov constant $C \cong 1.5$, which corresponds to the accepted value in classical turbulence [42].

The second one is the experiment on decaying quantum turbulence in He II generated by the towed grid. Various modifications of it have been performed over years by a Donnelly's group of in Eugene, Oregon. The essential experimental results have been published in a series of papers [43, 19, 18]. In these experiments, a grid was moved at constant speed up to 2 m/s through a channel of 1×1 cm^2 containing He II. The grid creates turbulence in both the normal and the superfluid components. Under assumption of homogeneity and isotropy, the measured excess attenuation of second sound provides information about the density of vortex lines (and thus vorticity, see later) in a small fixed region through which the grid had moved.

The figure 2.8 is composed in such a way that it displays all observed regimes of decaying vorticity in the grid generated He II turbulence. The early part of the vorticity decay displays a power law with exponent -11/10 and later -5/6. After saturation of the energy–containing length scale, typically over several orders of magnitude the decaying vortex line density, L, closely follows the power law with exponent -3/2, represented by the thick solid line. All the measured decay curves eventually closely follow this universal power laws behavior, in accord with the classical spectral decay model for decaying homogeneous and isotropic turbulence in a finite channel. The very late decay can be characterized as exponential one, of a form $exp\,(-t/t_0)$.

In order to compare the decay of classical grid turbulence and the measured decay of L in the Oregon experiment, we have to discuss the role of quantized vortices in He II turbulence. The simplest system to assimilate the role of quantized vortex lines is a rotating bucket of He II. In steady state, the normal fluid is in solid body rotation. As was mention in earlier the superfluid imitates solid body rotation and evolves to match the vorticity of the normal fluid.

Similarly to how vortex lines align themselves in a rotating bucket, bundles of quantized vortices align on the cores of normal fluid eddies. The superfluid vorticity is comparable to the vorticity of the normal fluid eddy and the effective fluid density is equal to the total fluid density. In a turbulent flow there will be a complex tangle of vortices

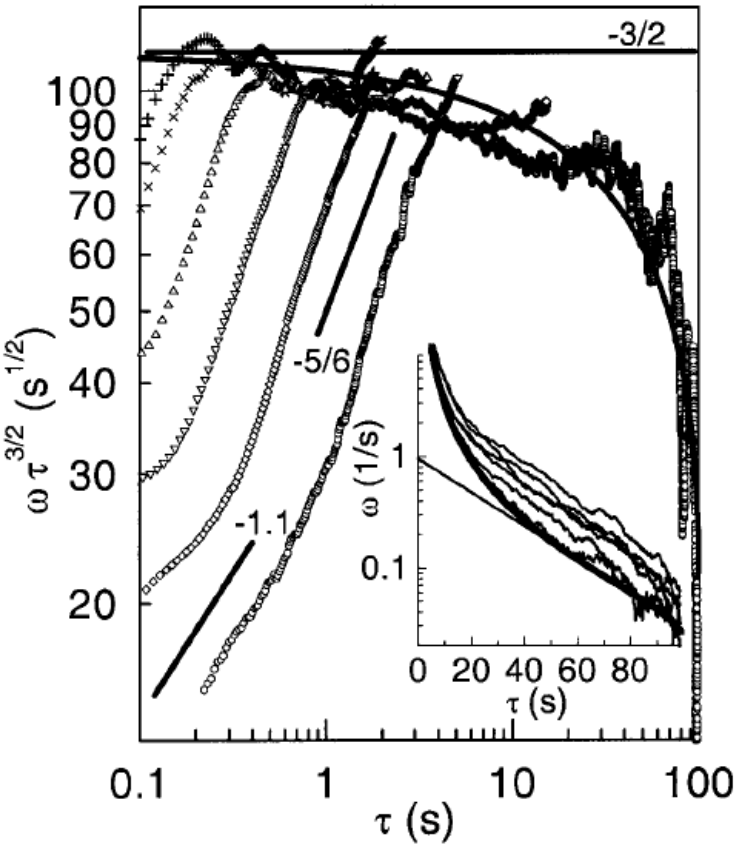

Fig. 2.8: The decaying vorticity multiplied by $(t + t^*)^{3/2} = \tau^{3/2}$, measured at T = 1.65 K. The early part of the decay displays power laws with exponents -11/10 and later -5/6, as indicated by straight solid lines next to the data sets. The influence of growing Kolmogorov length scale is indicated by the difference from the horizontal direction i.e., -3/2 power law. The inset shows the late decay which can be characterized as exponential, of a form $exp(-t/t_0)$ with t_0 = 29 s, represented by the straight solid line.

evolving in such a way as to minimize the difference between the two otherwise independent velocity fields. Turbulent He II flow thus resembles classical flow possessing an effective kinematic viscosity ν_{eff} of order η_n/ρ, where η_n is the dynamical viscosity and ρ denotes the total density of He II. If so, then the mentioned above usual homogeneous and isotropic turbulence relationship should apply:

$$\varepsilon = -\frac{dE}{dt} = \nu_{eff}(T)(\kappa L)^2 \,, \tag{2.31}$$

i.e., vorticity would be defined as κL.

The underlying physics of Eq. 2.31 is discussed in detail by [44, 45]. On length scales large compared with the mean vortex line spacing, l, the two fluids are likely to be coupled together by the mutual friction force and to behave like a conventional fluid with

non-dissipative motion. There is a dissipation on a scale of order, l, given by Eq. 2.31, taking into account that $L \propto l^{-2}$ is the length of vortex line per unit volume. On smaller length scales account must be taken of dissipation, due to viscosity in the normal fluid, frictional interaction between the vortex lines and the normal fluid, and the radiation of sound from the vortex lines. Motion on the largest length scales contains most of the turbulent energy, as it is described by the Kolmogorov spectrum. Energy flows from the large length scales to smaller ones in a cascade, energy from the largest eddies flows continuously to those in which dissipation takes place ($k \sim l^{-1}$). On some length scale the two fluids must become decoupled. The total energy flux:

$$\frac{dE}{dt} = \frac{dE_s}{dt} + \frac{dE_n}{dt} \,, \tag{2.32}$$

where dE_s/dt and dE_n/dt are energy fluxes in the superfluid and normal fluid per unit volume, respectively. Then assuming fully coupled motion of superfluid and normal fluid ($v_s = v_n$) we find that the total rate at which energy is flowing down the combined cascade per unit volume is given by

$$\frac{dE}{dt} = \frac{\rho}{\rho_s}\frac{dE_s}{dt} \,, \tag{2.33}$$

The total rate of energy loss per unit mass of helium, ε, is given by

$$\varepsilon = -\rho_s \kappa \alpha \left\langle v_L^2 \right\rangle L \,, \tag{2.34}$$

where α is the mutual friction coefficient and $\langle v_L^2 \rangle$ denotes an average of local velocity over vortex tangle. However, in Eq. 2.34 L is the length of vortex lines per unit volume relating to a random tangle. But in grid turbulence the tangle is partially polarized in order to create the large-scale motion. So we have to reduce the effective value of L by factor of s, of order unity.

According to the local induction approximation each element of vortex line moves with velocity given by

$$v_L = \frac{\kappa}{4\pi R} \ln\left(\frac{R}{a_0}\right) \,, \tag{2.35}$$

where R is the local radius of curvature and a_0 is an effective core radius. In the Schwarz theory [46] the ratio between the curvature of the vortex lines and the line spacing is given by

$$\left\langle \left[\frac{1}{R^2}\right] \right\rangle = c_2^2 L \,, \tag{2.36}$$

It follows that

$$\frac{dE}{dt} = \frac{s\kappa^3 \alpha c_2^2}{16\pi^2} \left(\ln \frac{R}{a_0}\right)^2 L \,. \tag{2.37}$$

We note that Eq. 2.37 has the same form as Eq. 2.31, and therefore the decay can also be expressed in terms of an effective kinematic viscosity, given by

$$\nu_{eff} = \kappa \left(\frac{s\alpha c_2^2}{16\pi^2} \right) \left(\ln \frac{R}{a_0} \right)^2 . \tag{2.38}$$

As one can see in Fig. 2.9, this model calculation correctly predicts the tendency for $\nu_{eff}(T)$ and roughly agrees with experimental results that have been obtained [47] by comparison of the experimental data with the spectral decay model prediction for the third universal regime

$$L(t) = \frac{(3C)^{3/2} D}{\kappa \nu_{eff}^{1/2}} (t - t^*)^{-3/2} \tag{2.39}$$

with the virtual origin time t^*, which for late decay time $t \gg t^*$ can be neglected.

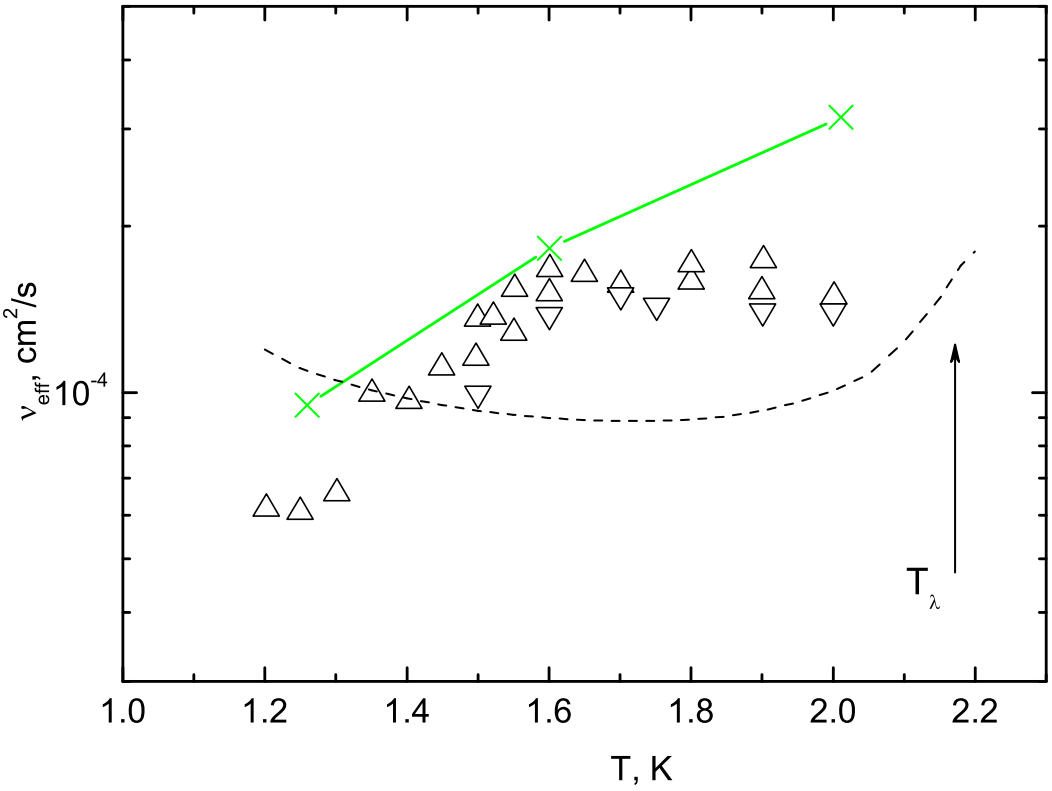

Fig. 2.9: The temperature dependence of the effective kinematic viscosity of turbulent He II above 1 K. Up- and down–triangles are deduced from the decaying vortex line density in the experiments with unconventional and conventional grids respectively. The crosses connected by the solid line represent a model calculation for $\nu_{eff}(T)$. The dotted line is a plot of kinematic viscosity of He II based on the total fluid density [28].

Fig. 2.9 shows that the extracted effective kinematic viscosity ν_{eff} has the same order of magnitude as η_n/ρ, but displays different temperature dependence. Let us stress that in view of the link between He II turbulence and classical turbulence, having in mind the possibility of practical use of He II as a working fluid [48], knowing the exact value of effective kinematic viscosity and its temperature dependence is essential.

We are left to discuss the last exponential part of the experimentally observed decay, for which the spectral decay model that assumes fully developed turbulence cannot be used any more. With no inertial scale left there is no energy transfer toward higher wavenumbers and the only possibility for further decay is the exponential viscous decay. This is the fourth and last regime of decaying vorticity in a finite channel. The late decay curves originating from various Re_M (see inset on Fig. 2.8) display an exponential decay of the form $\omega \propto exp(-t/t_0)$ (practically indistinguishable from the spectral model prediction). This last decay regime can be considered in analogy with the decay of the oscillatory motion in viscous fluids, characterized by exponential decay of the energy $E \propto E_0 \mathsf{exp}(-\beta t)$, where the decay coefficient $\beta = 3\nu k^2$. For $k = 2\pi/D$ and ν of order 10^{-4} cm^2/s it suggests a characteristic decay time close to the observed one.

2.5.4 Decay of Counterflow Turbulence

For several years our laboratory investigated decaying counterflow turbulence in two channels of square cross-section and in one cylindrical channel [22]. A typical family of decay curves measured at 1.6 K is shown in Fig. 2.10.

It was found that the decay of turbulence generated by a heat flow can be divided in two stages. After the heater is switched off the liquid cannot become isothermal instantly. So, during the first stage, before time ($t < t_s$), the liquid is not isothermal yet. The initial decay of the steady-state counterflow turbulence is taking place under conditions that the turbulence is still partly thermally driven, by the excess heat energy which is present in the the hotter part of the channel near the heater. However, in the second stage ($t > t_s$) the liquid can be considered as approximately isothermal and the decay as free. The time t_s depends on the channel's length and geometry as well as on experimental conditions.

We concentrate here on the isothermal stage of the decay, which in turn consists of an early part, where depolarization of vortex tangle and growth of the energy containing length scale takes place [34, 35] and a late power law decay. It was found that this late part of the decay (*past saturation time* t_{sat}) displays the classical $t^{-3/2}$ power law (see Fig. 2.10), independent of temperature over the range of investigation, despite the con-

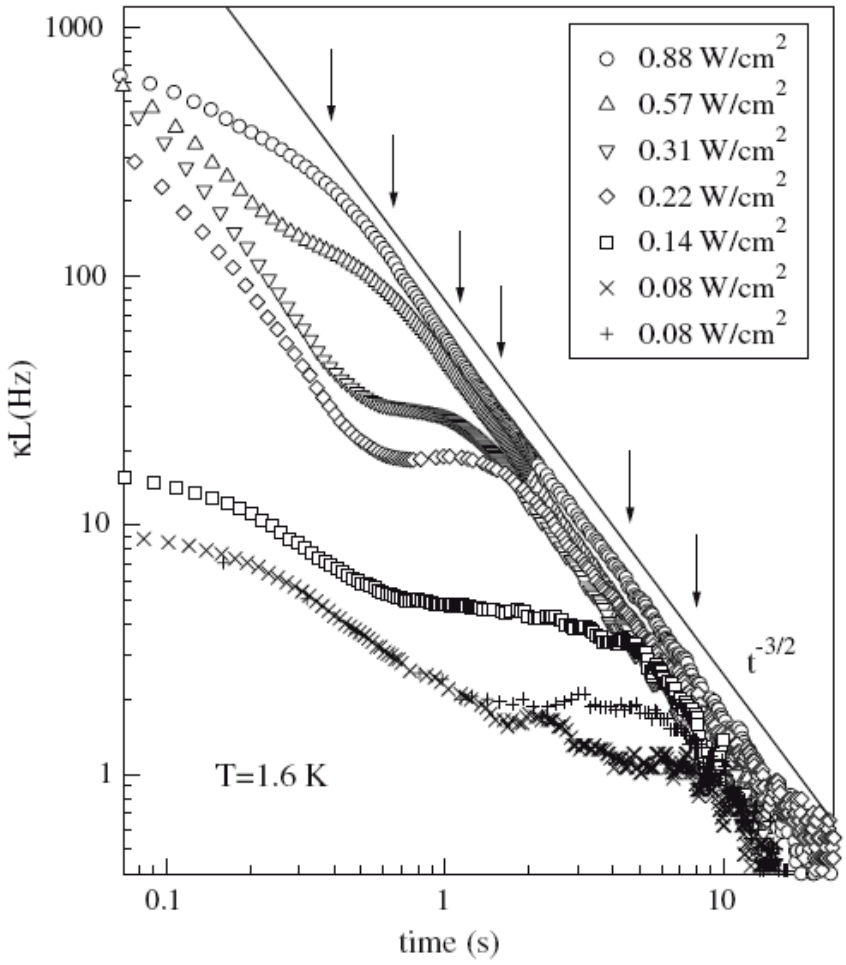

Fig. 2.10: The decay of vortex line density in counterflow turbulence measured at 1.6K for various initial heat inputs as indicated. The saturation times, t_{sat}, after which the decay displays classical character of the form $t^{-3/2}$ are marked by arrows.

siderable change of the superfluid to the normal fluid density ratio. We remind that the same temperature independence was observed in the decay of turbulence generated by a towed grid. These results strongly suggest that for $t > t_{sat}$ the decay of counterflow turbulence and the decay of grid-generated turbulence are essentially similar and follow the pattern predicted by the phenomenological spectral decay model [38] discussed above.

Moreover, the measurement of decaying counterflow turbulence provided a first direct experimental check that the vortex line density in the late stage of the decay is proportional to the channel size d, in accord with Eq. 2.39 (see Fig. 2.11). This result confirms the surprisingly close similarity between the late stage of decaying counterflow turbulence in He II and the decay of classical homogeneous and isotropic turbulence.

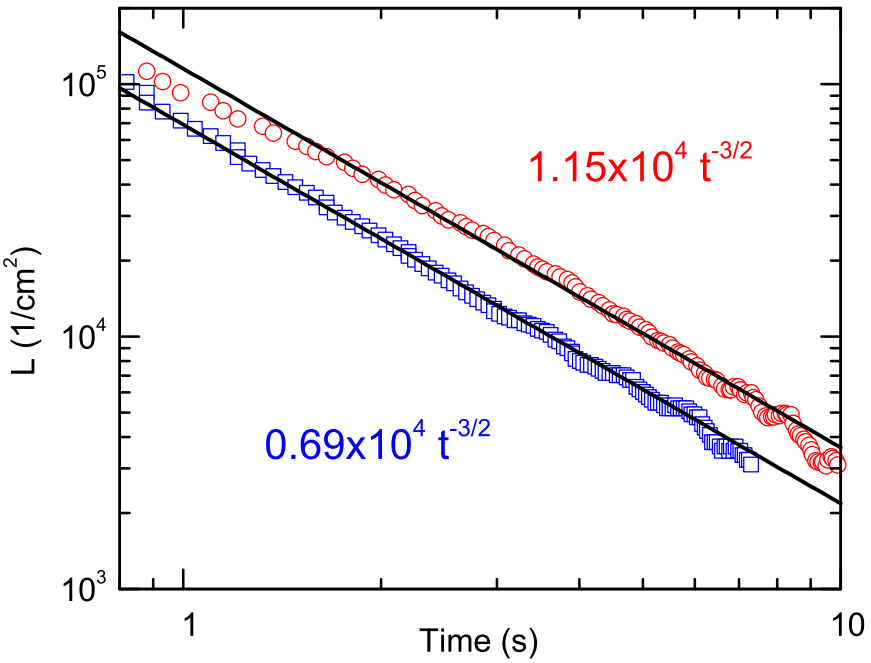

Fig. 2.11: The decaying vortex line density at 1.5 K calculated using formula Eq. 2.39 from the second sound data measured in both channels assuming that the decaying turbulence is homogeneous and isotropic. The third universal decay regime (the power law decay with the exponent of -3/2 represented by solid line) is reached irrespectively of the initial conditions from steady-state counterflow. The decay data measured in the 0.6×0.6 cm^2 channel (blue squares) follow the third universal decay regime but with the prefactor lowered by 0.6, the ratio of the channels widths, in comparison with the decay data measured in the 1×1 cm^2 channel (red circles), in accord with Eq. 2.39.

We stress that this result was very unexpected. Back to the Vinen equation (Eq. 2.16), there is the analytical solution [30], which for a particular case of free decay reduces to the inverse time dependence of the form

$$L(t) \propto \frac{1}{t + t_{vo}}\,, \tag{2.40}$$

where t_{vo} stands, as usually, for the virtual origin time. The physical meaning of t_{vo} is the instant from when L would have decayed from infinitely large value. We see, however, that this simple inverse time prediction of the Vinen's equation does not describe the experimental data for decaying counterflow turbulence in He II.

Chapter 3

Experimental Setup and Protocol

3.1 Experimental Setup and Equipment

For observing various types of He II flow we have used a standard stainless steel HK150 open bath cryostat. Natural ^{4}He is used as refrigerant as well as the working fluid. Our experimental setup is of flexible construction, allowing us to use several cells to generate and probe various flows of He II [P4]. The vapor above the liquid surface can be pumped out and, as a result, temperature of the entire helium bath decreases. We have used a powerful pumping unit based on the CIT Alcatel RSV 350 roots pump that allows to lower the temperature down to about 1.35 K.

The experiments described in this Thesis have been carried out in two brass channels 11.5 cm long, of square 6×6 mm^2 and 10×10 mm^2 cross-sections (see Fig. 3.1). For experiments on thermal counterflow one end of the channel was dead and contained a manganin wire heater wound on a cone. The author of this Thesis took part only in the final part of the counterflow experiments and in the data analysis, but had a full responsibility to design and manufacture the experimental setup used for investigation of quantum turbulence generated by pure superflow. The experiment can be characterized as follows.

Both ends of the brass flow channel are blocked by sintered silver superleaks about 3 mm thick and 16 mm in a diameter[1]. They are embedded inside brass flanges and smoothly connected to the channel via a thin In O-ring. Large diameter of the superleak and filling factor of the finest silver powder to about $1/2$ of the bulk density of silver ensure that the superfluid can freely penetrate through such superleaks and thus through

[1]These superleak were sintered at Institute of Scientific Instruments, AS, CR, Brno by J. Dupak in situ directly in the brass flanges.

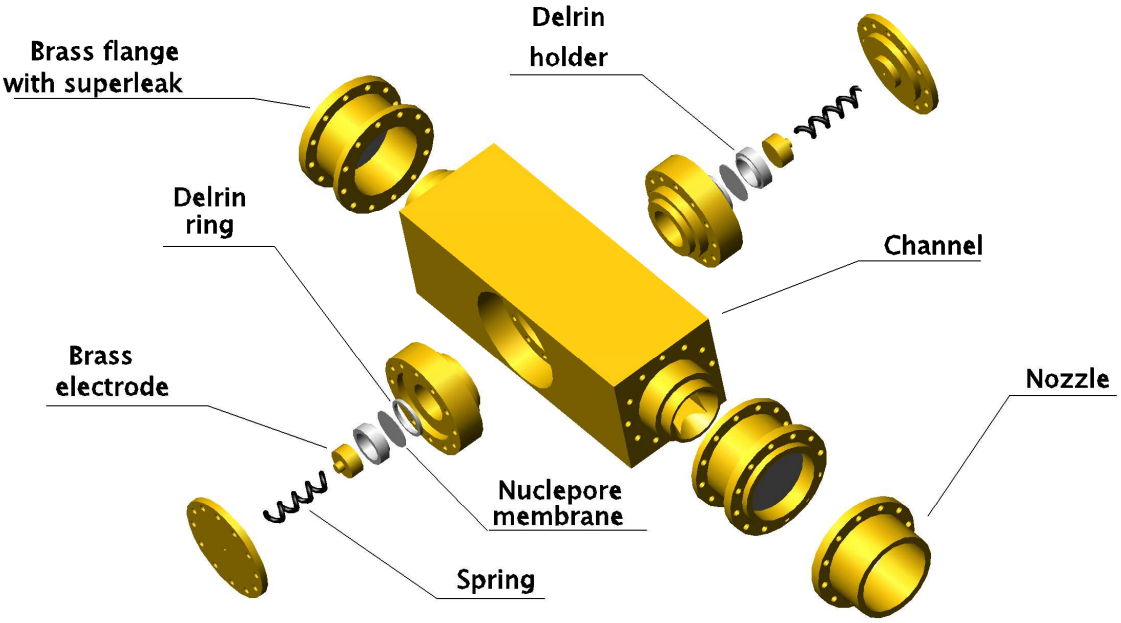

Fig. 3.1: Shematic picture of the channel.

the channel, but superleaks stay opaque for the normal fluid.

Prior incorporating the superleaks in the experimental setup, we have successfully tested the analogical one (prepared using exactly the same technology) in a separate experiment, by utilizing the famous "fountain" effect[2].

The brass channel body with attached via thin indium O-ring superleaks is mounted to the stainless steel tube shaft and positioned vertically inside the cryostat. Additionally, a brass "nozzle" is fixed on the top of the upper superleak. The bifilarly wound manganin 50 Ω heater H1 (see Fig. 3.2) is placed inside the nozzle above the upper superleak. The heater has a distributed spiral form in order to ensure uniformity of the supplied heat over entire crossection of the superleak. Another heater, H2, with matched resistance value is placed in the bath so that the externally applied power can be easily switched from one heater to another. This helps to avoid temperature fluctuations when flow in the channel is triggered or stopped. The procedure of power switching between heaters H1 and H2 is based on the National Instruments data acquisition device (NI-DAQ) and the home-made Power Split Unit (PSU) designed and manufactured for us by Ing. Frantisek Soukup, a member of the Joint Low Temperature Laboratory. NI-DAQ sends the

[2]This effect, in principal, can be used to measure velocity of the superfluid, namely, by measuring the height of the fountain stream.

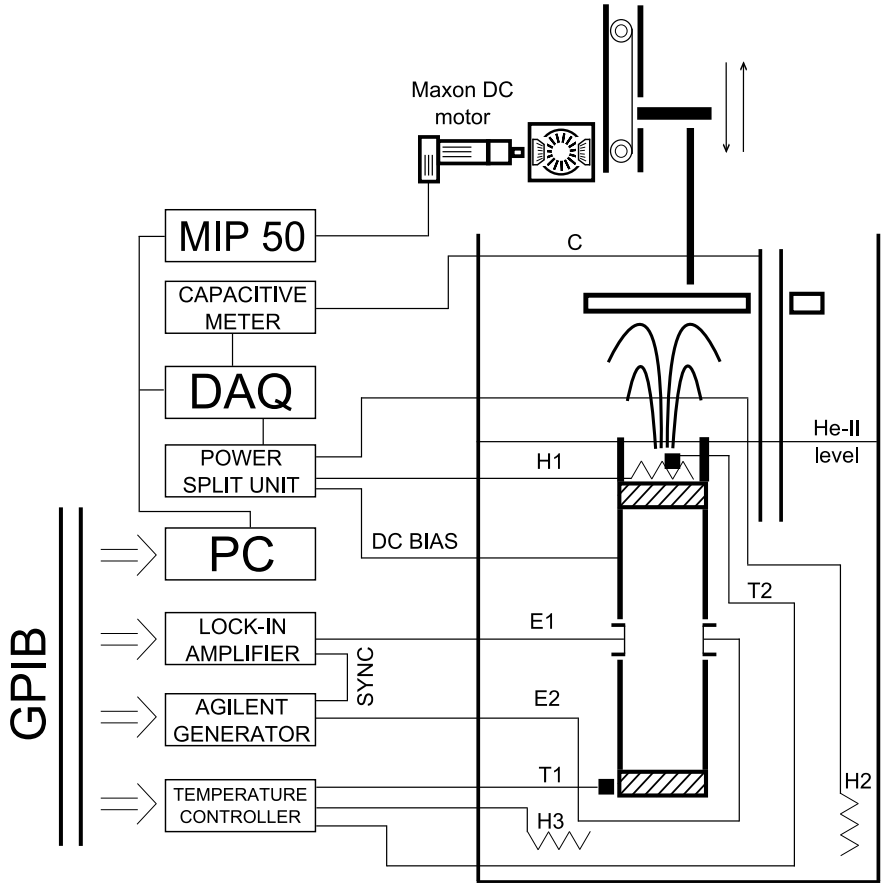

Fig. 3.2: Principle circuitry of the experimental setup.

reference signal to the amplifier input of the PSU (of maximum value 2 V). This signal is proportional to the output current which the amplifier applies to the channel and bath heaters. The total heat power applied to the system is kept constant. We have typically used heat powers to our system up to about 0.4 W; above this value it proved difficult to stabilize the temperature with the desired accuracy (which depends on experimental conditions and roughly means that the corresponding frequency shift of the second sound resonance is much smaller than its linewidth).

Yet another 50 Ω heater, H3, is mounted on a plastic plate on the bottom of the cryostat, serving as a tool for fine temperature stabilization of the helium bath. Its temperature is monitored and controlled by by the Conductus LTC-21 temperature controller, via the calibrated Cernox sensor T1, or via the Ge film on GaAs thermometer T2 [49].

In order to spend all the heat from the channel heater on generation of a flow through the channel, the only thermal contact between the channel heater and helium in the bath must be through the helium inside the channel. Technically this was made in such a way that the top edge of the channel is positioned slightly above the liquid surface. On

the other hand, if the channel heater in the nozzle were not covered by liquid helium, it would be impossible to create any flow through the channel.

To ensure that the fountain pump outlet is positioned at the same level above the surface of the liquid in the helium bath represents an experimental challenge, as the helium level of the pumped open bath is dropping during the experiment. We have solved this using a home-made capacitance level sensor **C**, which is mounted in parallel to the channel. It consists of three coaxial stainless steel tubes, 3 mm, 6 mm and 9 mm in diameter. The two inner tubes are used as a capacitor and the outer one as a shield. The useful signal from this sensor in helium is very small, of order *(fF/mm)*. For measuring such a small signal we had to design and manufacture a special Capacitance Meter *(it was designed by Ing. Frantisek Soukup)*. The level stabilization process is as follows: The NI-DAQ transforms the analog signal from this device and sends it to PC. The computer calculates the required vertical displacement (from the pre-set value) of the channel with respect to the helium level in the bath and through the MIP-50 board sends commands to the Maxon DC motor. The Maxon DC motor performs required number of steps and changes the vertical position of a lift system attached to the shaft to which the channel is mounted inside the cryostat, so that the He–level in the nozzle above the upper superleak stays constant during the experiment. The lift and gear system have been designed, constructed and mounted on a special platform at the top of the cryostat. A stainless steel rod (30 cm long, 5 mm in diameter) with a good polished surface is screwed to the lift. It passes through a special vacuum tight flange, which is fixed on the top of the main flange of the cryostat. This vacuum tight flange consists of a tube with two rubber O-rings. The space between the O-rings can be either pumped out or overpressurized by helium gas, in order to prevent contamination of the helium bath by air during experiments. The Maxon DC motor is connected to the gear system. The requested values of velocity and acceleration of the lift motion are set up by the MIP-50 board connected through COM port to computer. It allows setting up a lift motion velocity about 0.1 mm/s. The other end of the rod is screwed to a thin-walled stainless steel tube (90 cm long and 9 mm in diameter) equipped with a plate for mounting the flow channel on the opposite side inside the cryostat. The vertical position of the entire cryogenic inset can be changed within 20 cm range; the channel can move vertically very slowly and accurately, without perturbing the helium system. To calibrate the Capacitance level meter, we performed a special experiment which will be described in subsection 3.1.2.

3.1.1 Second Sound Sensors

Second sound attenuation is a powerful tool for experimental investigation of quantum turbulence in He II. In order to generate and detect second sound wave, we designed and produced various types of second sound sensors. Construction of the holder and sensors size depends on the type of experiment and experimental cell.

In the present experiment we used sensors 10 mm in diameter, with the holder made a of special strong and highly isolating material Delrin. Both the transducer and receiver sensors are based on a gold-plated Nuclepore membrane. The membrane has very fine submicron pores and one side of it is covered by about 100 nm thick layer of gold. We have designed and manufactured a special holder for the membrane and gold-evaporating of our membranes has been done in the Institute of Physics ASCR, with kind help of Jarmila Prachařová. With the help of especially designed tools the circular piece of the gold-plated membrane is punched out, carefully stretched over a plastic 10 mm cylindrical ring and fixed by another plastic Delrin ring (see Fig. 3.1). Care is taken to avoid any wrinkles on the stretched membrane surface that would lead to non-uniform generation of second sound. The sensors are placed opposite each other across the channel, buried in its body in the middle of its length. There are small lugs inside holes and gold-plated membrane surface placed inside has an electrical contact with the channel body. The surface of the sensor membrane is thus fixed almost flush with the inner wall of the channel. This way any additional perturbation concerning non ideal geometry of the channel is minimized and the cross section of the main flow along the channel stays fixed. Both holes drilled for sensors – transducer and receiver – into the brass channel body are then tightly closed by brass discs via In O-rings. The iron spring is fixed on the inner side of each brass disc; its opposite end is connected via an insulator to the brass electrode, mechanically pressed to the insulating side of the sensor membrane. The sensor holes have to be tightly closed by brass discs mounted via In O-ring to avoid any helium leak from the bath so that the superfluid can enter the channel only through the bottom superleak. To a good precision, its mean velocity can be calculated from the known heat power applied to the fountain pump heater.

The gold-plated side of the nuclepore membrane in combination with the brass electrode over which the membrane is stretched makes a capacitor. The DC BIAS, typically up to 100 V, is applied to the channel body and used to press the membrane against the brass electrode more tightly. The capacitance of these sensors reaches typically 60 - 80 pF, while the sensitivity threshold at a working frequency of order 1 kHz is about 1 fF. In order to avoid additional noise from the connecting leads we use the high quality

Lake Shore cryogenic coaxial cable with no appreciable microphone effect and miniature LEMO coaxial vacuum-tight connectors.

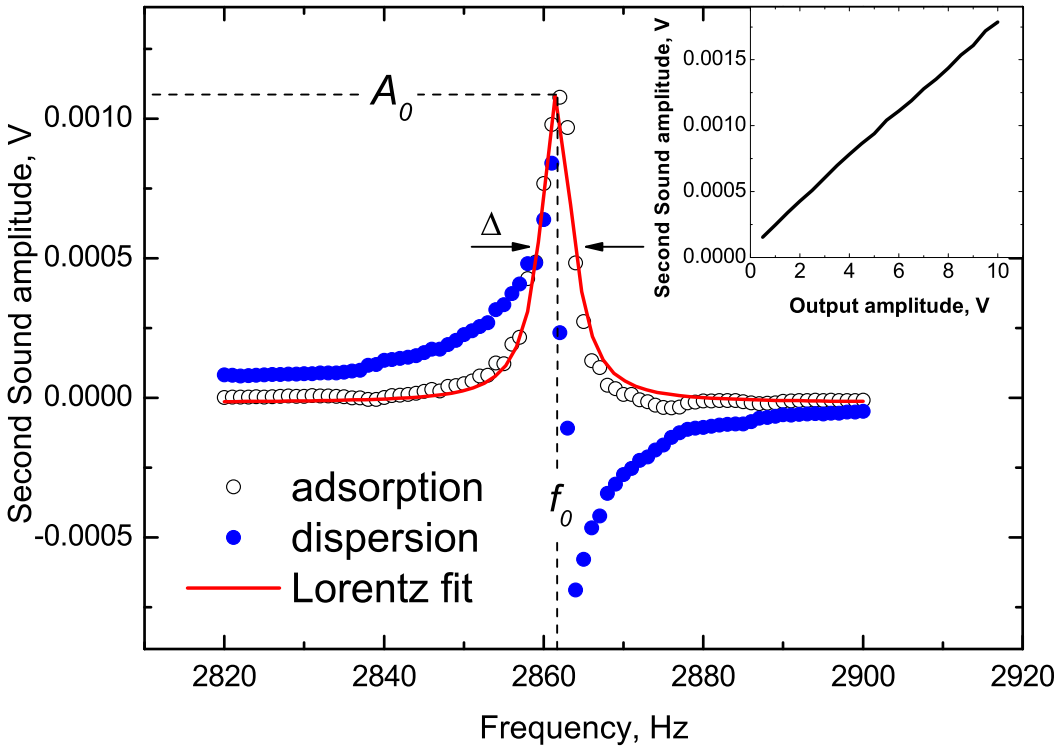

Fig. 3.3: The form of the second sound signal plotted against frequency, showing the absorption (empty symbols) and dispersion (filled symbols) data with no power applied to the fountain pump (no flow). The red curve is a fitted Lorentzian. A_0 is the second sound amplitude (SSA) at resonance frequency f_0 and Δ is the full width of the peak at the half height. Almost linear dependence of the SSA signal versus the drive amplitude at the frequency of resonance (see insert) proves that second sound sensors themselves do not create any quantized vorticity in the channel.

The mechanism of generation and detection of a second sound wave in our experiment utilizes antiphase oscillations of normal and superfluid components. The membrane begins to oscillate after applying the sinusoidal driving signal to the transducer. It forces the membrane to meve and it pushes the normal component whereas the superfluid component can freely penetrate and stays basically motionless. The space between the transducer and receiver acts as a second sound resonator. On the opposite side of the channel, the normal component pushes the receiver membrane. For detecting this signal electrically, we use the SR 830 dual phase lock-in amplifier. The sinusoidal driving signal is generated by the Agilent 33250A function generator. It generates the excitation signal

up to 10 V pick–to–pick in 0.001 V steps in the frequency range from 1 Hz to 10 MHz. Thus slowly sweeping the frequency of the driving signal we observe second sound resonance peaks nearly Lorentzian in shape (see Fig. 3.3). It is possible to calculate their resonance frequencies as $\nu^{-1} = nl/V_{ss}$, where l is the distance between membranes, V_{ss} is the velocity of second sound and n is number of the half–wave lengths of the second sound signal for the observed resonance mode. Typically we have used harmonics with resonant frequencies lying between 1 kHz and 3 kHz.

3.1.2 Capacitance helium level meter tuning procedure

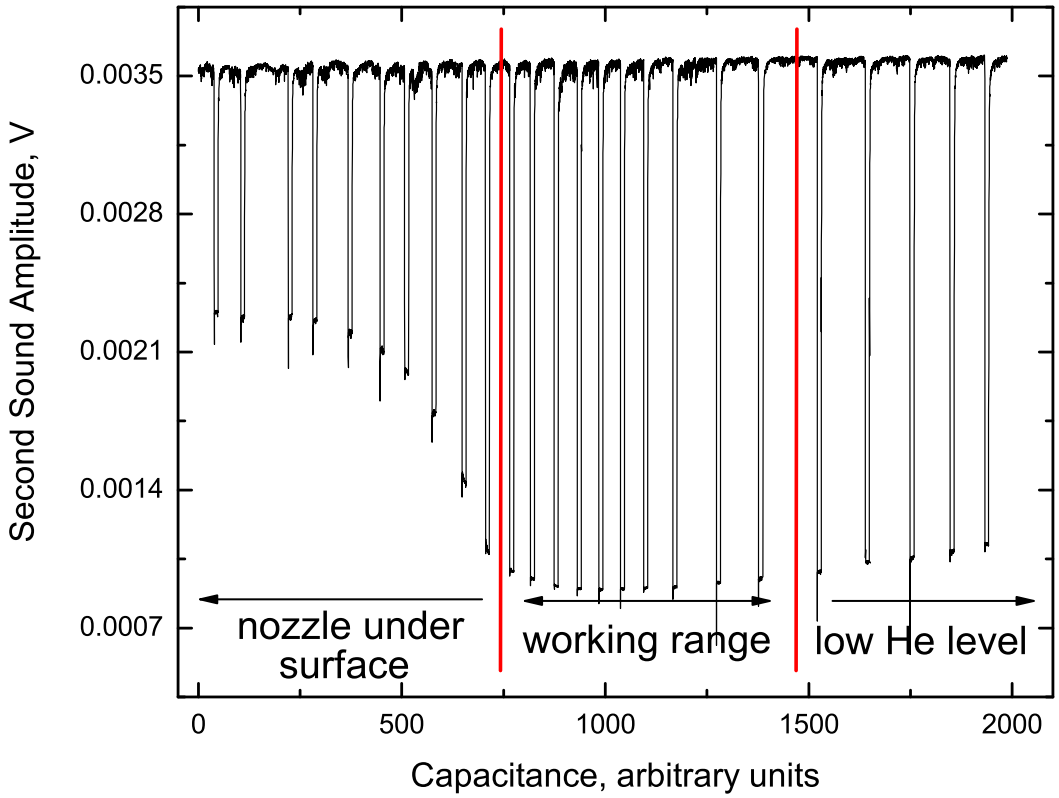

Fig. 3.4: The capacitance helium level gauge calibration data. There are three ranges divided by red lines. Left: The channel is entirely submerged below the He II surface; middle: the top of the nozzle is above the liquid level (working range); right: the heater H1 is already in the vapor and thus in a weak contact with He II – SSA will increase with dropping of helium level in the bath.

As we have already mentioned, we use the home–made capacitance meter as a helium level indicator in our experiments. In order to find the best working level within

the acceptable vertical level range for actual measurements, we use the following tuning protocol.

By applying current to the heater H1, we aim to force the superfluid to flow due to the temperature gradient. We stress that the normal fluid is not able to penetrate the superleak. If the top end of the channel (i.e., the outlet of the fountain pump) is entirely submerged under the liquid level in the bath, the applied heat propagates from H1 in all available directions and superfluid flows to the heater through the channel as well as directly from the bath. Thus the main flow through the channel is weak; with small number of created vortices. On the other hand, when the channel heater is entirely above the liquid surface, the supplied heat to H1 propagates through the poorly conducting helium gas. It means that in this case the number of created quantized vortices is much smaller than when the entirely submerged heater has a good contact with the highly conducting superfluid liquid. In both cases (outlet of the fountain pump submerged or heater H1 above the liquid surface) precise calculation of the flow velocity through the channel based on the known heat power supplied to the fountain pump heater H1 is not possible.

For calibration, we sank the channel and found second sound resonance peak which corresponds to the vortex free conditions. Applying high enough heat pulse a dense vortex tangle is created resulting in decreasing of the observed second sound amplitude. Minimum values of SSA mark the position of the channel within an acceptable working range. Calibration data are presented in figure 3.4.

3.2 Steady-state and decaying turbulence

All our standard devices such as the Conductus LTC-21 cryogenic temperature controller, the SR 830 dual phase lock-in amplifier, the TD 2000 Tektronix Oscilloscope, and the Agilent 33250A function generator are controlled via the GPIB bus card by PC, using the NI LabView software. All the multifunctional LabView software that includes setting up the initial conditions, controlling of the experimental run and reading out the raw measured data has been created by the author of this Thesis.

The measurements have been performed in two independent modes: (i) steady state measurements and (ii) measurements of decaying turbulence. In both modes, it is essential that the temperature of He II bath is kept constant during the run. Fine stabilization of the temperature is achieved by the LTC 21. For various temperatures, we found the most appropriate PID scheme. The vertical position of the channel relative to helium

surface was always kept within the working range. The observable quantities were the current applied to the heater H1, the readings of thermometers T1 and T2, the frequency and amplitude of the second sound driving signal and (the principal measured quantity) the amplitude of the second sound receiver in the vicinity of the chosen second sound resonance peak.

3.2.1 The steady-state measurements

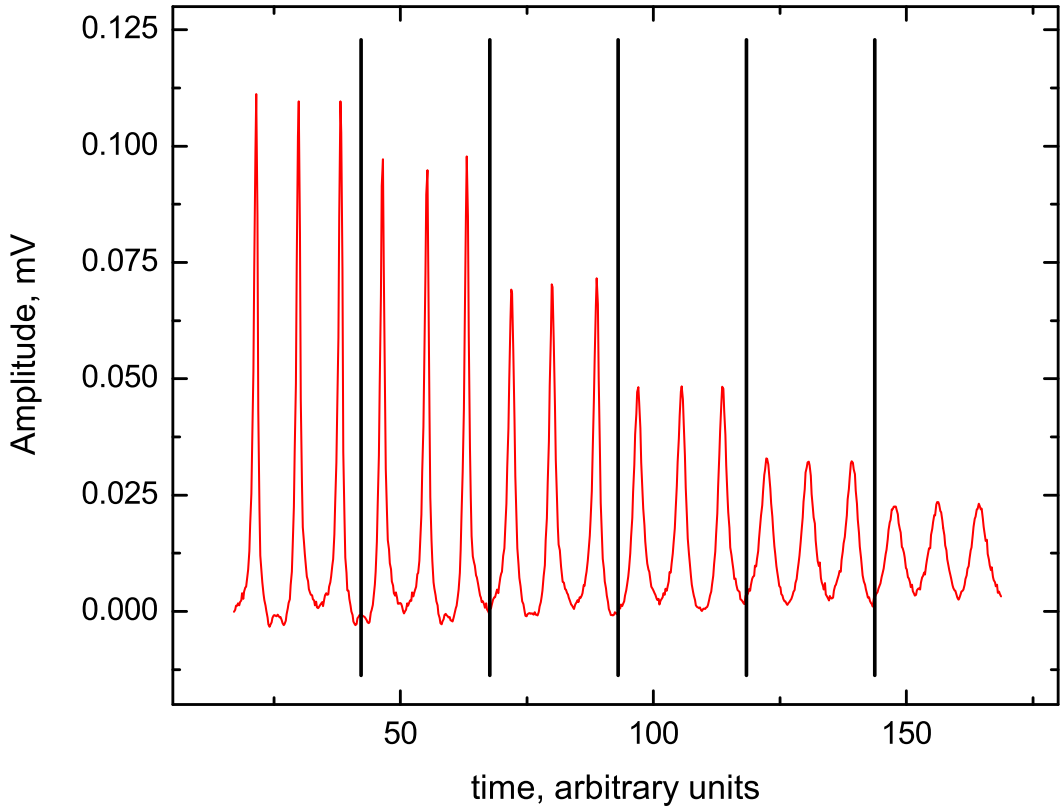

Fig. 3.5: The example of raw data for steady-state measurements: the top of the chosen second sound resonance peak is scanned in both directions, then the applied heat to the fountain pump is changed.

In this type of experiments, we scanned the frequency of the driving signal applied to the transducer over the chosen (typically second) second sound resonance peak several times for each fixed heat applied to the heater H1. Typically at the beginning of the run, we additionally measured SSA without any heat input to H1, for detecting the undisturbed second sound amplitude A_0 and the width of the peak Δ (see Eq. 4.6). Then the heat power was subsequently increased by the preset step and the peak was scanned for

several times in both directions (for detecting the suppressed amplitude A). As the observed stabilization time of the steady state flow in our channel is several seconds, we did not scan whole peak and limited the scan by several Hertz around its resonance frequency. Normally the heat power was changed from the lowest value to the highest one. Measurements in opposite direction are more difficult, because stabilization takes more time owing to long decay time of pinned vortices inside the channel. In this case, values of SSA are typically somewhat higher, especially in the low heat power range. An example of raw data is presented in Fig. 3.5. Using such sets of data, it is possible to calculate the vortex line density and using the values of the current supplied to the heater H1, also the mean velocity of the superfluid component flowing upwards through the channel.

3.2.2 The decay measurements

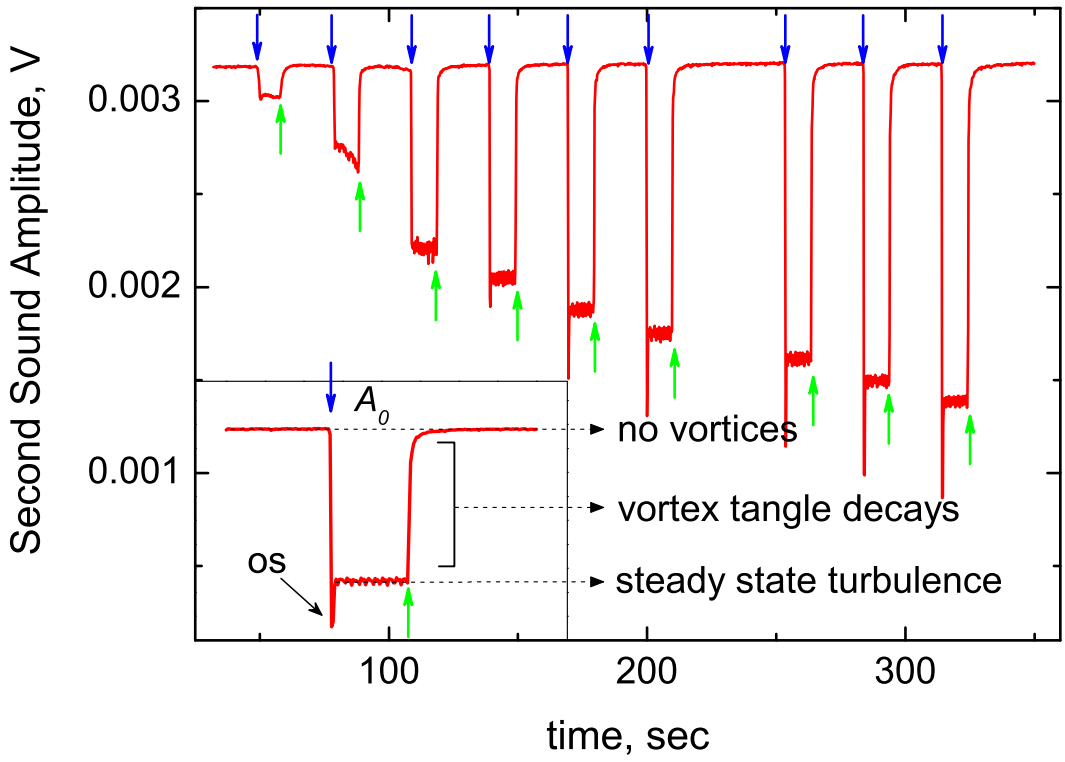

Fig. 3.6: Example of raw data on decaying turbulence, showing the typical behavior of the second sound amplitude at resonance - heater On (blue arrow): vortices appear and the second sound amplitude decreases. When the overshoot **os** is over, the system comes to the steady state regime. Heater Off (green arrow): turbulence decays and the second sound amplitude is recovering to its initial value A_0.

To detect A_0 and to be sure that it stays constant during the measurement we have

scanned the SS resonance peak both before and after each run. We had no time to scan the entire peak or even any part of it during the decay, because turbulence decays rather rapidly. Thus we find and set up the resonance frequency for each run and assume that it does not change during all manipulations. This assumption is reasonable, as the suppressed peak in the presence of turbulence in the channel is much wider and any small frequency shift would not result in appreciable reduction of the actual amplitude in comparison with that at true resonance. Additionally, we have experimentally checked by scanning over the suppressed peak in the steady-state regime that the possible frequency shift is in most cases indeed negligible.

After initial measurement of A_0 (about 15-20 sec) we stepwise switched parts of the power from the compensating heater H2 to the channel heater H1. The SSA immediately drops down and, after a short initial time (from 1 to 2 seconds), it stabilizes on a new level. From this moment on the superfluid flows through the channel in the steady state regime. We kept the flow in steady state regime for typically about 10-20 seconds, then the theater H1 was switched off and we observed relaxation of the SSA to the initial value A_0. Figure 3.6 shows evolution of the second sound amplitude for one such a run.

Chapter 4

Experimental results

In this Chapter, we describe only selected results needed for self-containing description of the physics underlying our pure superflow and thermal counterflow experiments. Inclusion of all available results will make the Thesis too bulky and more difficult to follow. For further details, we refer the reader to the already published papers.

4.1 Mean superflow velocity through the channel

In the present experiments we assume that the superfluid enters the channel through the bottom superleak, and that there is no net normal fluid through it[1].

For calculation of the mean superflow velocity through the channel we suggest the following reasoning. Knowing the electrical resistance of the fountain pump heater H1 and measuring the supplied current through it, we calculate the power $\dot{q} = \dot{Q}/d^2$ per unit cross-section of the channel, which we apply to the system. Here $\dot{Q}$ is the applied heat power and d is the size of the channel. The power $\dot{q}$ is the only source of energy, the principle part of it is spent at the heater H1 on conversion of the superfluid into the normal fluid. In principle, we have also to add the kinetic energy of the normal flow $\rho_n v_n \frac{v_n^2}{2}$ and the kinetic energy of the superflow $\rho_s v_s \frac{v_s^2}{2}$, having in mind that $\rho_n v_n$ and $\rho_s v_s$ are the mass flows of the normal fluid and of the superfluid, respectively. We can therefore write the following energy budget equation:

$$\dot{q} = \rho v_n ST + \rho_n v_n \frac{v_n^2}{2} + \rho_s v_s \frac{v_s^2}{2} \ . \tag{4.1}$$

Furthermore, we assume the fountain where superfluid and normal fluid velocities are matched: $v_n = v_s$. This assumption is justified, as we have independently checked by

[1] However, we can not exclude any motion of the normal fluid inside the channel.

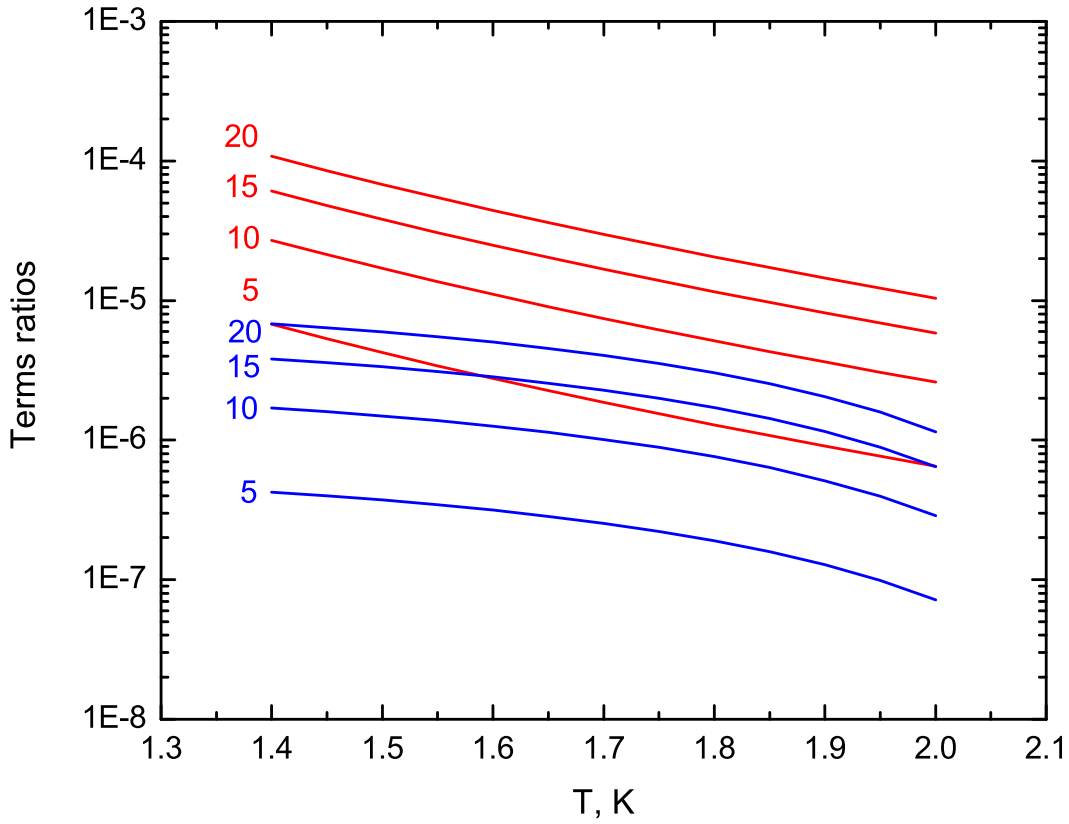

Fig. 4.1: Relative weights of the second (red line) and the third terms (blue line) of the RHS of equation 4.1 (in comparison with the first RHS term) as a function of temperature for various superfluid velocities as indicated.

direct measurements, using thermometers T1 and T2, that the temperature of the fountain is hardly different from that of the helium bath.

The numerical solution of equation 4.1 shows that the second and the third terms on the RHS are small (less then one percent) and can be neglected. Figure 4.1 presents the relative weights of the second and the third terms as a function of temperature for various superfluid velocities. Thus the total mass of helium leaving the channel every second equals:

$$M_{out} = v_n(\rho_s + \rho_n)d^2 = \frac{\dot{Q}}{ST} \; ; \tag{4.2}$$

where:

$$\dot{Q} = \dot{q}d^2 = \rho v_n STd^2 \; ,$$

with S denoting the entropy of He II. On the other hand, this must be the same mass as

that of the incoming superfluid via the channel:

$$M_{in} = v_s \rho_s d^2 \ . \tag{4.3}$$

Thus the mean superflow velocity in the channel can be expressed as:

$$v_s = \frac{\dot{Q}}{\rho_s S T d^2} \ . \tag{4.4}$$

It is fair to mention that there are other effects which could, in principle, influence the flow inside the channel, such as oscillations of the superfluid through superleak after the heater is switched off, pinned vortex lines, flow of the superfluid film over the nozzle, finite thermal conductivity of the brass and Kapitza thermal resistance, but it is difficult to take them into account quantitatively and according to our estimates we believe that they can be neglected. Note that all these effects would tend to slightly lower the mean superfluid velocity calculated above.

As for the experiments on thermal counterflow in which the author took part, we remind that the thermal counterflow was generated by a standard way, i.e., by applying a heat current, via a heater (resistor) located at the closed end of a channel with the opposite end open to the helium bath. The heat flux is carried away from the heater by the normal fluid alone. Assuming that the power $\dot{Q} = d^2 \dot{q}$ applied at the heater is used entirely to convert the incoming superfluid into the normal fluid, the velocity of the outgoing normal fluid is $v_n = \dot{q}/(ST\rho)$. The counterflow velocity v_{ns} is then easily established from the condition $\rho_s v_s + \rho_n v_n = 0$ and becomes equal to the mean superfluid velocity calculated above, i.e.:

$$v_{ns} = \frac{\dot{Q}}{\rho_s S T d^2} \ . \tag{4.5}$$

4.2 Vortex line density

To calculate the vortex line density from our second sound data, assuming that the vortex tangle is homogeneous and isotropic, we use the expression:

$$L = \frac{6\pi\Delta_0}{B\kappa} \left(\frac{a_0}{a} - 1 \right) \ , \tag{4.6}$$

where a_0 is the unperturbed second amplitude with no applied heat into the channel, Δ_0 is the full width at half hight of the second sound resonance absorption peak (typically 10 Hz) and B is the temperature dependent dissipational mutual friction coefficient. The experimental procedure how to obtain these quantities has been described in the previous Chapter.

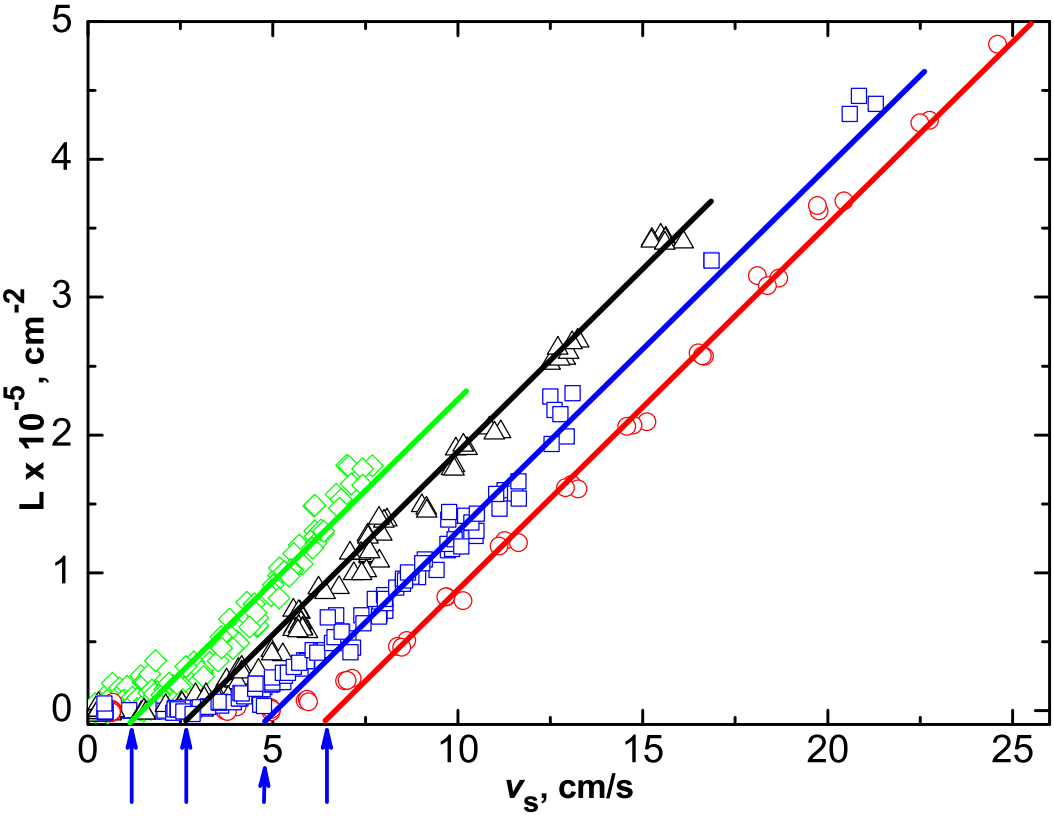

Fig. 4.2: The calculated steady-state vortex line density plotted versus the mean superfluid velocity in the 6 mm channel. The blue arrows from below indicate the fitting parameter – slip velocity $v_{\rm cr}^{\rm II}$; the solid lines (from left to right) are plots of linear dependencies $L = \beta(v - v_{\rm cr}^{\rm II})$ for the data sets taken at T=1.92 K, (green), T=1.73 K, (black), T=1.58 K, (blue) and T=1.49 K, (red), with $\beta = 2.65 \times 10^4$ cm^{-3}s.

4.3 Steady-state results

We have investigated the steady-state flow in two square channels at various temperatures in the range 1.45–1.95 K. Figures 4.2 and 4.3 illustrate the behavior of the flow, via the dependence of calculated vortex line density plotted versus mean superfluid velocity in both channels at various temperatures. Based on these data, we can identify three ranges corresponding to different types of flow (see Fig. 4.4).

The first range, which appears below the first critical velocity v_{cr}^{I}, is characterized by a constant – nearly zero – density of vortex line. We suppose that below v_{cr}^{I} the flow is nearly dissipationless and thus potential. Sometimes, by repeating the experiments, we observe low but non-zero value of the vortex line density even in this regime. We belive, however, that it is connected with pinning of quantized vortices, most likely on

Fig. 4.3: The calculated vortex line density plotted versus the main superfluid velocity at various temperatures as indicated, in the channel of 10×10 mm^2 cross-section.

the surface of superleaks and on the second sound porous sensors. Number of pinned vortices can vary a little in time even without any flow through the channel. Normal fluid stays quiescent in the first regime. Note that the first regime here differs from the first laminar regime in the thermal counterflow, where laminar flow of the viscous normal fluid causes finite dissipation already below the critical velocity.

The second range (A-state) appears above the critical velocity v_{cr}^I. The observed vortex line density grows here proportional to the square of the mean superfluid velocity and in analogy with the thermal counterflow can be described in terms of the mutual friction formalism [46]:

$$L^{1/2} = \gamma(T)(v - v_{cr}^I) \ , \tag{4.7}$$

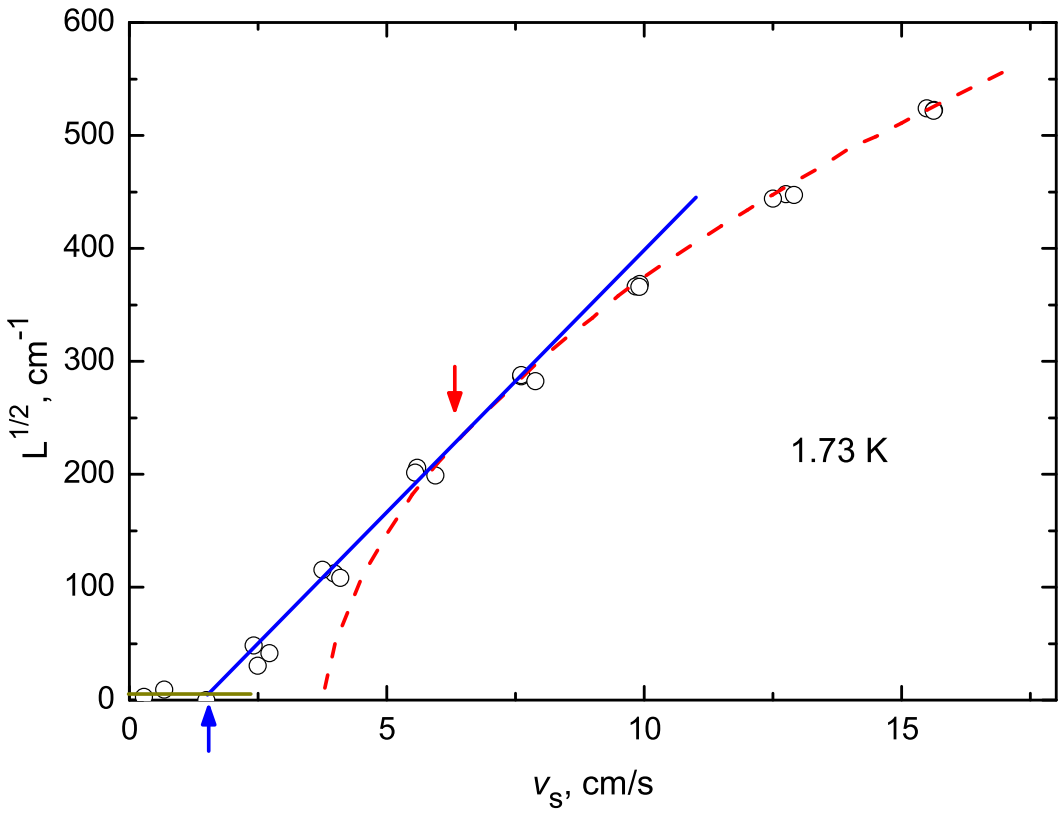

Fig. 4.4: The square-root of the vortex line density L as a function of mean superfluid velocity for channels 6×6 mm^2 (black circles) and 10×10 mm^2 (red squares) cross-section. Blue and red arrows show the first critical velocity v_{cr}^I and the loosely defined second critical velocity. There are three flow ranges fitted by: the brown line – the laminar flow, the blue one – the turbulent A-state and red dotted-line – the turbulent B-state.

where $\gamma(T)$ and v_{cr}^I are determined from the fits to the data. Dependencies of the γ coefficient versus temperature for both channels are presented in figure 4.5. As one can see, the γ coefficient increases with increasing temperature. The black dotted-line on figure 4.5 is $\gamma(T)$ from the Schwarz theory. Our experimental results are in qualitative agreement with this theory, but the actual values are lower by a factor of about three. One of the possible reasons of this discrepancy is that the vortex tangle in the A-state is not homogeneous and isotropic.

The behavior of the vortex line density in the A-state is therefore analogical to thermal counterflow, which was first investigated by Vinen [20, 26] and agrees with the prediction of the phenomenological Vinen equation discussed above. Such a flow was previously observed in our Laboratory in both present channels [50] when used without superleaks, in a regime of thermal counterflow. We did not measure steady state of counterflow in

a detail. However, the calculation of $\gamma(T)$, taking into account the error bars, is in the qualitative agreement (for counterflow $\gamma \approx 50$ at 1.7K) with γ coefficient in case of steady state of pure superflow.

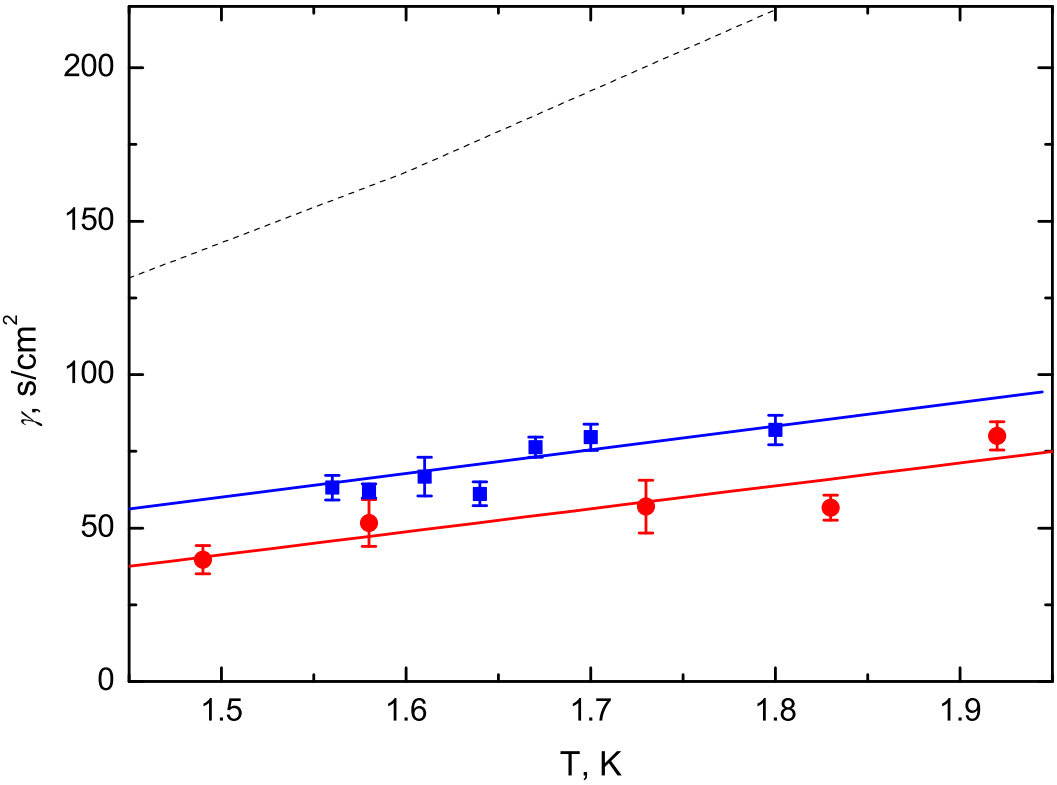

Fig. 4.5: Vortex line density coefficient $\gamma(T)$ in the A-state for both channels. Red circles and blue squares are the average values of the experimental data for channels of 6×6 mm^2 and 10×10 mm^2 cross-section, respectively. Red and blue straight lines are linear fits through these averaged values. The black dotted-line represents γ(T) from the Schwarz theory.

We emphasize that the A-state is the only one so far experimentally observed in pure superflow [24]. However, our results (see figure 4.2 and 4.4) show the dramatic modification, taking place at loosely defined second critical velocity, from the A-state to a newly discovered B-state, representing **the third range** of the flow.

The new B-state can be characterized by the linear dependence of vortex line density on the mean superfluid velocity, of the form

$$L = \beta(v - v_{cr}^{II}) \,, \tag{4.8}$$

where β and v_{cr}^{II} are fitting parameters, physical meaning of which will be given below.

Figure 4.6 shows β as a function of temperature. We see that β has very weak, if any, temperature dependence. The spread of β points as well as in values of critical velocities v_{cr}^{I} and v_{cr}^{II} is connected at least in part with the time interval allowed in the measurement for setting up the steady-state regime. If the time between the two subsequent steady-state measurements is too short, the new steady-state value of L becomes slightly shifted. This might be connected with the pinning-depinning processes inside the channel, where the configuration of pinned vortices did not fully relax to the new steady-state level.

The important experimental observations are that within the investigated temperature range the character of the flow in the B-state hardly changes with temperature and that the A-B transition is gradual, as one can see from figure 4.4.

The turbulent B-state was clearly observed only in the smaller 6×6 mm^2 channel. The reason of this is experimental: the mean superfluid velocity is inversely proportional to the cross-section of the channel. In order to go deep enough inside the B-state in the larger 10×10 mm^2 channel, one needs to apply rather high power to the fountain pump. The temperature stabilization is difficult under these conditions which results in a drift of the resonance frequency of the second sound peak and measurements can be only qualitative. Nevertheless, we have clear qualitative indication that the A-B transition occurs in the wider 10 mm channel as well.

Figure 4.7 shows the critical velocities v_{cr}^{I} and v_{cr}^{II} versus temperature. The first critical velocity, v_{cr}^{I}, is observed to be only weakly temperature dependent in both channels (taking into account the error bars, in the first approximation it can perhaps be considered as constant), while v_{cr}^{II} decreases with decreasing temperature rather more steeply.

4.4 Results on decaying vortex line density

Our sensitive second sound attenuation technique is capable of investigating not only the steady-state quantum turbulence in He II, but also its temporal decay - an interesting phenomenon in itself. Furthermore, investigation of decaying turbulence can help us to understand the underlying physics of the two experimentally observed turbulent steady-states A and B.

Figure 4.8 displays a family of decay curves originating from various high steady-state levels of vortex line density in the 6 mm channel. Let us stress that this character of the decay does not change with temperature, at lest over the entire range that we investigated. Over a complicated initial part of the decay, within about 1 s since the heater H1 was switched off, the decay gradually becomes exponential in character, of the

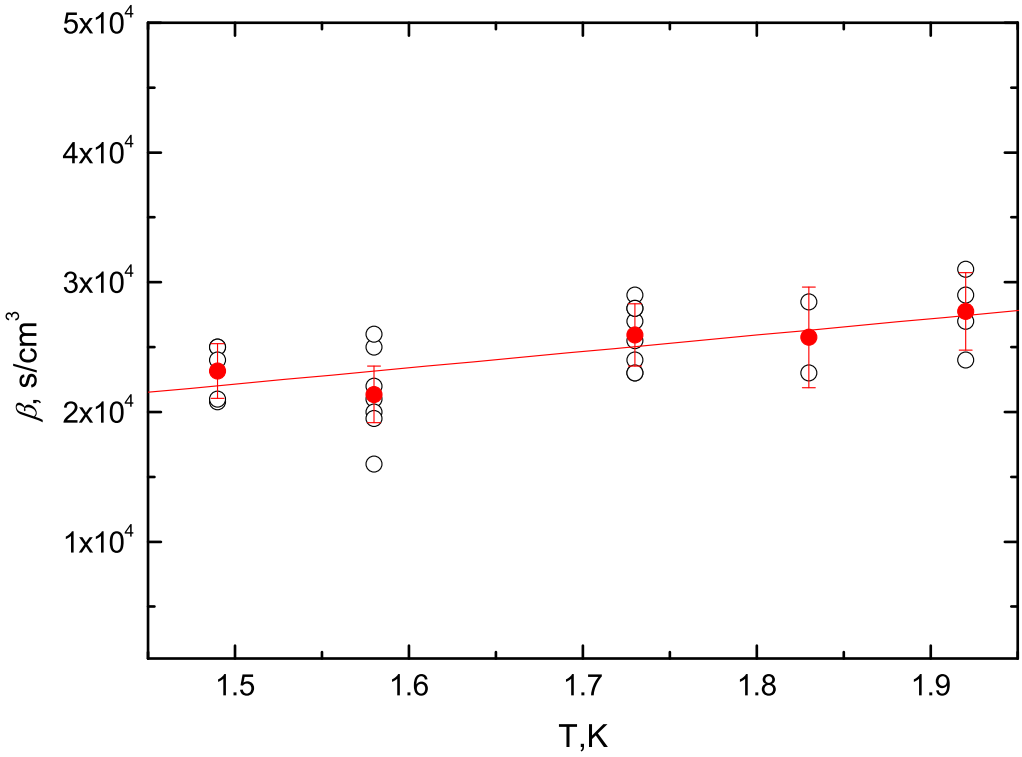

Fig. 4.6: Plot of the vortex line density coefficient $\beta(T)$ in the B-state versus temperature for the 6×6 mm^2 channel. Red full circles represent the averaged values of the experimental data at that temperature; the Red line is a linear fit through these averaged values.

form

$$L(t) = L(0)\exp\{-\frac{\mathrm{t}-\mathrm{t_{vo}}}{\tau}\}\,, \tag{4.9}$$

where t_{vo} is the virtual origin time – its approximately inverse proportionality on the mean superfluid velocity (as qualitatively observed at all temperatures) is shown in Fig. 4.9. The physical meaning of t_{vo} is to take into account the instant from when L would decay exponentially from an infinitely large value.

Analysis of the data shows that the characteristic decay time τ does not depend on the steady-state value of L from which the decay originates (providing that L is high enough, thus corresponding to the turbulent B-state) and only weakly on temperature (see Fig. 4.10). The rather large error bars are given, due to sensitivity of τ to a_0, which is reproducible only within about 1%, presumably due to trapped vorticity in porous membranes.

Let us mention here that the described character of the decay is distinctly different from our initial expectations based on known results on the decay of L in thermal counterflow [22] and [P3], where the decay is of complicated form (described in detail in previous

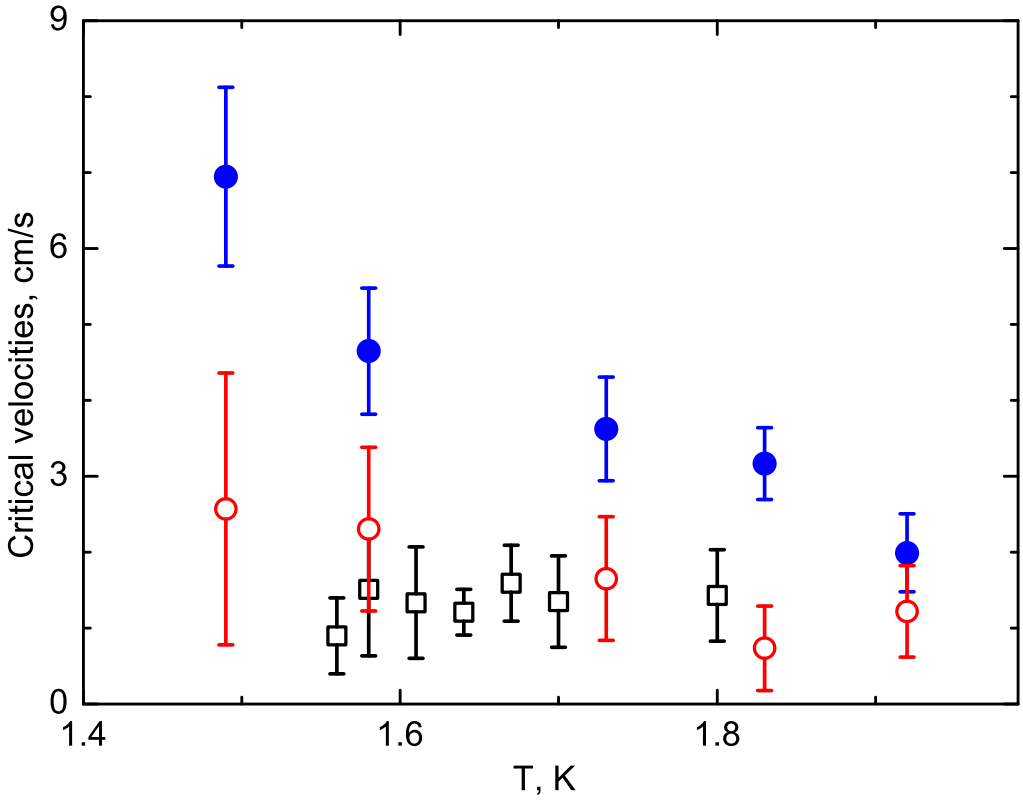

Fig. 4.7: The observed critical velocities v_{cr}^{I} and v_{cr}^{II} plotted versus temperature. Values of v_{cr}^{I} are given for both channels (open black squares - 10 mm channel, open red circles - 6 mm channel), while values of v_{cr}^{II} (filled blue circles) could have been deduced quantitatively only for the smaller 6×6 mm^{2}channel.

publications based on the experimental research performed in our Laboratory [34, 35]) but its late stage can be described by a power law with the classical exponent of -3/2 [P2, P5]. For completeness, let us add that the exponential decay of L was previously already observed, but only as a very late stage, for very low vortex line density part of the complex decay of the classically generated grid turbulence, consisting of four distinctly different regimes [18]. On the first sight, it seems therefore that our new unexpected result contradicts many earlier results obtained in thermal counterflow and strongly suggests that the nature of He II turbulence generated by superflow (namely the B-state) differs from that generated by the thermal counterflow.

This fact naturally invokes a question - are the decays originating from described above steady-states A and B different in character? To answer this question experimentally, it is best to compare the decay originating deep in the B-state in the 6 mm channel with that originating from A-state in the 10 mm channel, as here the A-state holds up to

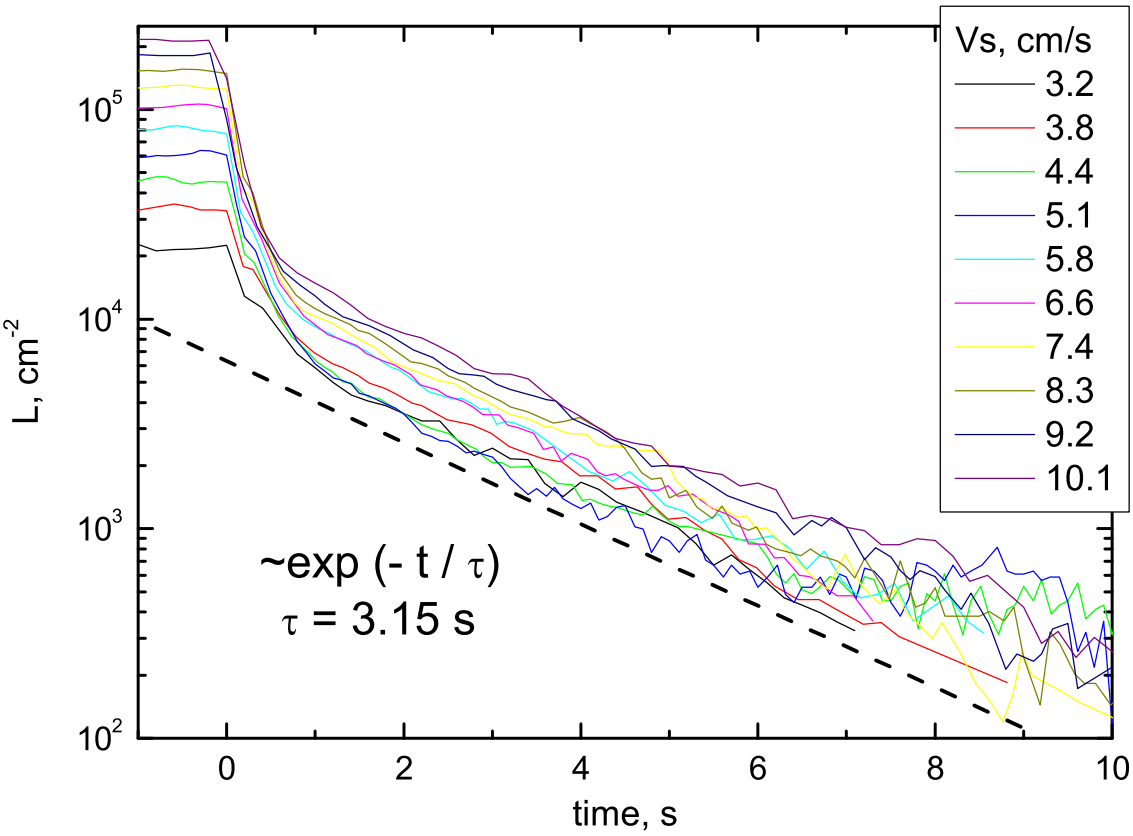

Fig. 4.8: Steady-state and decaying vortex line density (assuming that the vortex tangle is random) generated by pure superflow of various mean velocity. The displayed vortex line density is measured in the middle of the length of the 6 mm channel at T = 1.73 K. The heater is switched off at t = 0. Following the fast initial decay (past $\simeq$ 1 s), the exponential decay of the form $\sim \exp(-\mathrm{t}/\tau)$ is observed.

high enough steady-state values of L allowing long enough time over which the decay could be clearly resolved. Indeed, as illustrated in Fig. 4.11, the decay of the vortex line density originating from the A-steady-state in the channel of 10×10 mm^2 cross-section within certain limited parameter range displays about an order of magnitude of the expected classical power law dependence $L \propto t^{-3/2}$. The experimental answer therefore is that the character of the decay depends on the nature of the steady-state it originates from. Decaying A-state and B-state must therefore involve distinctly different underlying physics.

Due to the fact that we cannot penetrate deep enough into the newly discovered B-state (for reasons discussed earlier), we show no measurements in 10 mm channel originating from higher L than those given in Fig. 4.11. We restrict ourselves by saying that the measured decays can be considered as preliminary and qualitative only, they are of

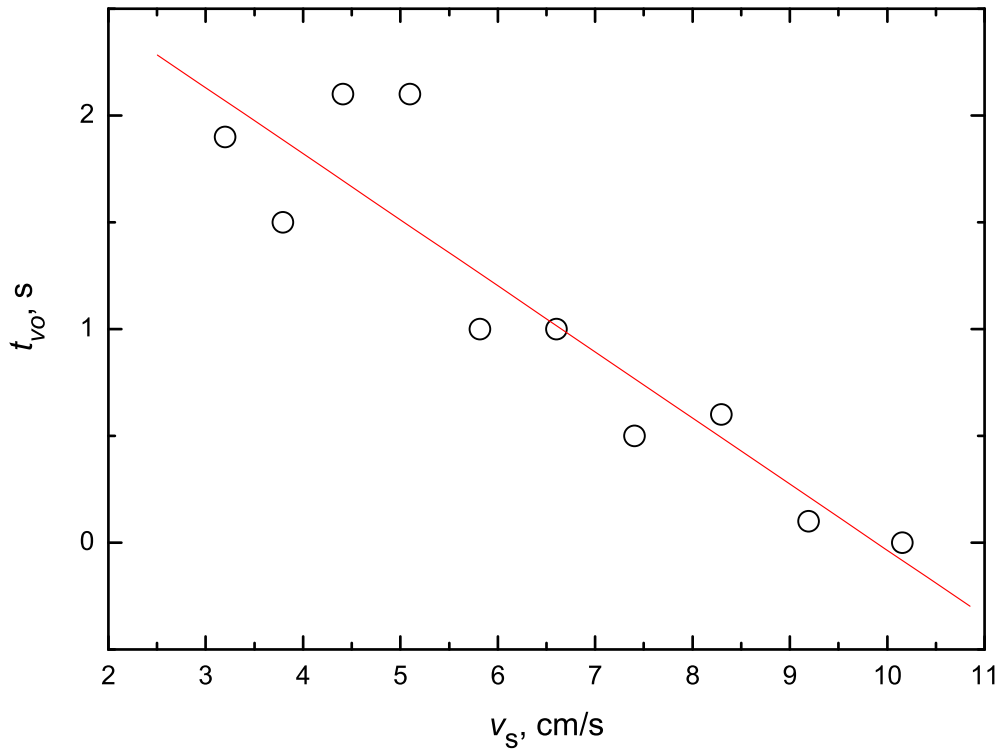

Fig. 4.9: Dependence of t_{vo} vs v_S for the 6 mm channel at T = 1.73 K.

more complex form and are substantively more difficult to interpret.

4.5 Results on decaying thermal counterflow

As it was already mentioned, the author of this Thesis took active part in experiments on thermal counterflow, performed prior experiments on pure superflow using the same two channels (without superleaks, placed horizontally in the helium bath, with one end open to the helium bath and the other (dead end) equipped by a resistive heater wound by the manganin wire on a brass cone to generate the studied thermal counterflow), especially on measurements of the decaying thermal counterflow. Here we present selected experimental results on the decaying thermal counterflow, which are in a close relationship with the already described results on decaying pure superflow. We shall skip description of first two stages of the decaying counterflow and concentrate on the third, universal decay regime, which in analogy with the classically generated grid turbulence in He II can be described quasiclassically, using the purely classical spectral decay model based

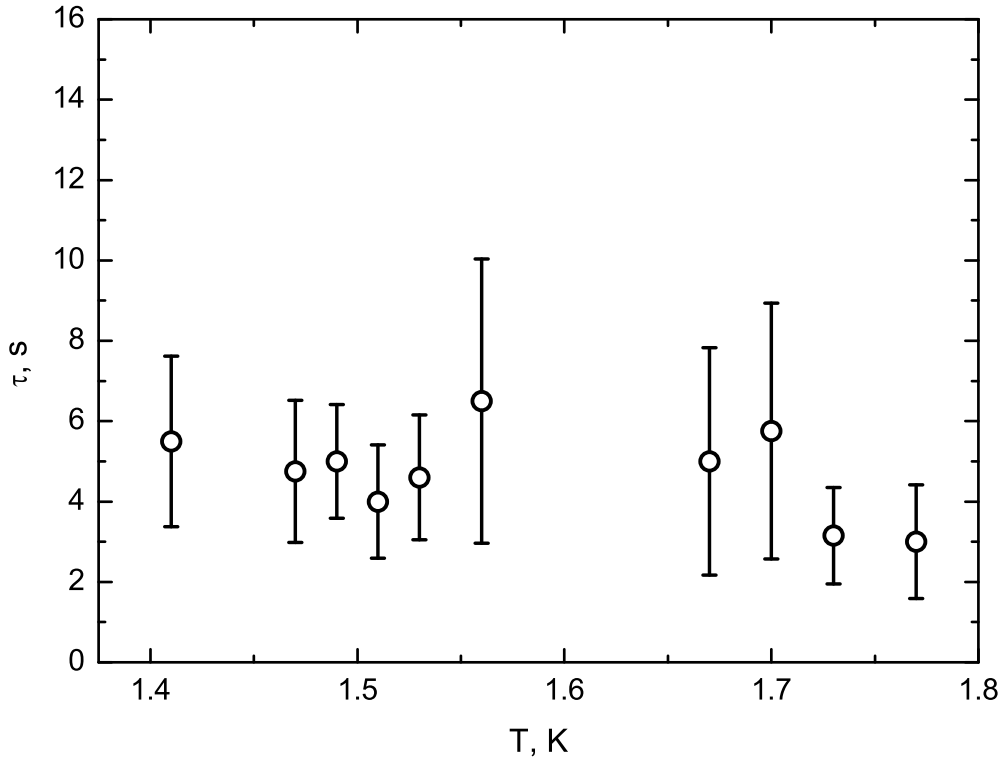

Fig. 4.10: Dependence of the decay time τ vs temperature for the channel of 6× 6 mm^2 cross-section.

on the accepted Kolmogorov K41 form of the classical 3D energy spectrum, predicting:

$$L(t) = \frac{d(3C)^{3/2}}{2\pi\kappa\sqrt{\nu_{eff}}}(t + t_{vo})^{-3/2} \cong \frac{d(3C)^{3/2}}{2\pi\kappa\sqrt{\nu_{eff}}}t^{-3/2}\,. \tag{4.10}$$

Some typical examples of the decay data are shown in Fig. 4.12. The top and middle frames show the quantity $a(0)/a(t) - 1$ versus time, measured in the 10 mm channel. As it was described in the previous Chapter, under assumption of homogeneity and isotropy this quantity is proportional to the vortex line density in the channel. As it was discussed in detail in [34, 35], during the first two stages of the decay the assumption of isotropy and homogeneity is not satisfied, however, as the decay progresses, the vortex tangle depolarizes and during the third universal stage of the decay it can be assumed to be, at least approximately, homogeneous and isotropic.

Fig. 4.12 clearly demonstrates that, although the decay curves measured at $T = 2$ K and at $T = 1.6$ K originate from the steady-state counterflow generated by applying various heat power and thus from different L, the third regime is universal in that all data eventually collapse on a single line given by formula 4.10.

The right frame of Fig. 4.12 displays the decaying L calculated from the second sound

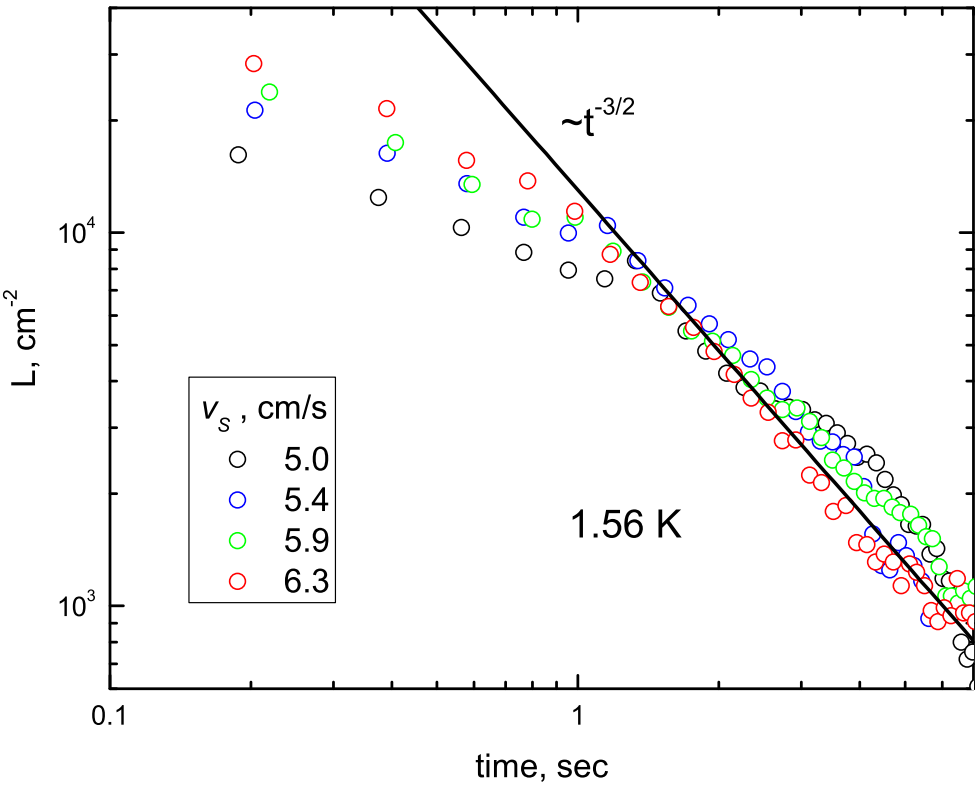

Fig. 4.11: Decaying vortex line density in the 10 mm channel originating from steady-state values of vortex line density generated at T = 1.56 K by the mean superflow velocities as indicated.

data measured in both channels at $T = 1.5$ K assuming that the decaying turbulence is homogeneous and isotropic and clearly shows once again that the third universal decay regime (the power law decay with the exponent of -3/2 represented by dashed lines) is reached irrespectively of the initial conditions. The decay data measured in the 0.6×0.6 cm^2 channel (filled blue symbols) also follow the third universal decay regime but with the prefactor lowered by the factor of $0.69/1.15 \cong 0.6$ - the ratio of the channels widths and therefore in full agreement with formula 4.10. To the best of our knowledge, it for the first time that formula 4.10 has been experimentally verified also with respect to the channel size, d.

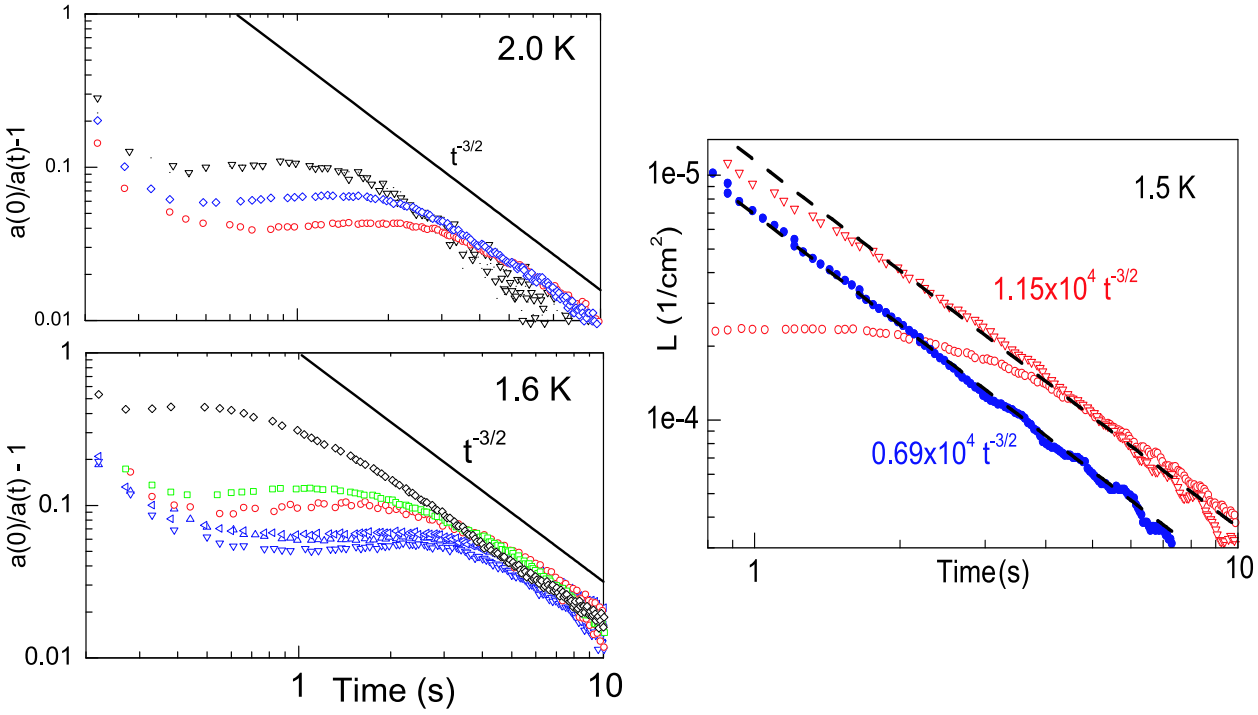

Fig. 4.12: Examples of the second sound experimental data. The top and bottom left figures show the quantity $a(0)/a(t)-1$ versus time, measured in the 1×1 cm^2 channel. The decay curves measured at $T = 2$ K originate from the steady-state counterflow generated by applying 0.52 W (∇), 0.41 W (blue $\diamond$) and 0.32 W (red $\circ$); the decay curves at $T = 1.6$ K from 0.5 W ($\diamond$), 0.23 W, (green squares) 0.18 W (red $\circ$) and 0.14 W (various blue triangles – three individual decay curves are shown to appreciate the level of reproducibility for the lowest applied power). The right figure shows the decaying L calculated from the second sound data measured in both channels assuming that the decaying turbulence is homogeneous and isotropic.

Chapter 5

Discussion

We shall start the discussion with considering the decaying counterflow, in order to build up the notion of an effective kinematic viscosity of turbulent He II. We shall show that under certain circumstances turbulent He II (i.e. containing the tangle of quantized vortex lines) can be treated, at least approximately, as a quasi single component quasi-viscous fluid, as motion of the superfluid and of the normal fluid on all relevant length scales (i.e., normal and superfluid eddies of all sizes present in turbulent He II) can be thought as tightly coupled together by the action of the mutual friction force. The decay of such a single component quasi-viscous fluid then can be considered fully classically, simply by replacing the kinematic viscosity of a classical viscous fluid by the effective kinematic viscosity.

Exactly this approach was successfully applied to understand the underlying physics of the decaying grid-generated turbulence in He II [19, 18], where it was assumed that normal and superfluid eddies are tightly coupled all the time, at all relevant length scales and normal and superfluid velocity fields being fully identical.

In case of **steady-state** counterflow or **steady-state** pure superflow this approach is not applicable, as there is a net counterflow velocity, which tries to tear apart the normal and superfluid eddies. As it was shown by Vinen [20, 26], eddies larger than certain critical size (that is given by the balance between the size of the eddy over its turnover time and the counterflow velocity) cannot be coupled. In counterflow, the mutual friction force is capable of coupling only eddies that are smaller than this critical size. On the other hand, in the **decaying counterflow turbulence** the net counterflow velocity quickly disappears. The critical size of normal and superfluid eddies that become coupled together therefore increases and over later stages of the decay the situation might closely remind that of decaying classically generated (e.g., grid) turbulence. To confirm this scenario

experimentally, we start our discussion with the decaying counterflow data.

5.1 Discussion on decaying counterflow

Let us consider results of counterflow experiments performed by the previous graduate student of our group A.V. Gordeev together with the author of this Thesis. We remind that these counterflow experiments have been performed using the same two channels of square cross-section (without superleaks). We have already discussed in the previous Chapter that the decaying vortex line density originating from various levels of steady-state counterflow turbulence displays the third universal decay regime, over which the vortex tangle could be assumed homogeneous and isotropic. The temporal dependence of this third universal regime of the decay follows the prediction of the classical decay model for vorticity in a finite size channel if He II is considered as a single fluid with an effective kinematic viscosity $\nu_{eff}(T)$. Moreover, measurements of the decaying counterflow turbulence in two channels of different square crossection provided the first direct experimental check that the vortex line density in this stage of the decay is proportional to the channel size, d, in accord with Eq. 2.39 (see Fig. 2.11) [P3]. This result confirms the surprisingly close similarity between the late stage of decaying counterflow turbulence in He II and the decay of classical homogeneous and isotropic turbulence.

5.1.1 Effective kinematic viscosity of turbulent He II

Thanks to the fact that decaying counterflow turbulence and grid generated turbulence are of so similar nature, it is possible to calculate the effective kinematic viscosity by comparing the experimental decay data of L measured at various temperatures using Eq. 2.39 [P6]. The results of our analysis for both channels of square crossection are displayed in Fig. 5.1. We found the values of $\nu_{eff}(T)$ calculated separately for two square channels within the experimental error overlapped, so effective kinematic viscosity does not therefore depend on the channel size. We have therefore calculated the mean values of $\nu_{eff}(T)$ over our new data from both channels at each temperature, represented in in Fig. 5.1 by the open diamond with error bars.

This set of the data has to be compared with $\nu_{eff}(T)$ obtained in the Oregon towed grid experiments. Such a comparison is justified and useful, as in the Prague counterflow experiments we have used the same square 1×1 cm^2 channel (plus the smaller one 0.6×0.6 cm^2) and essentially the same second sound technique.

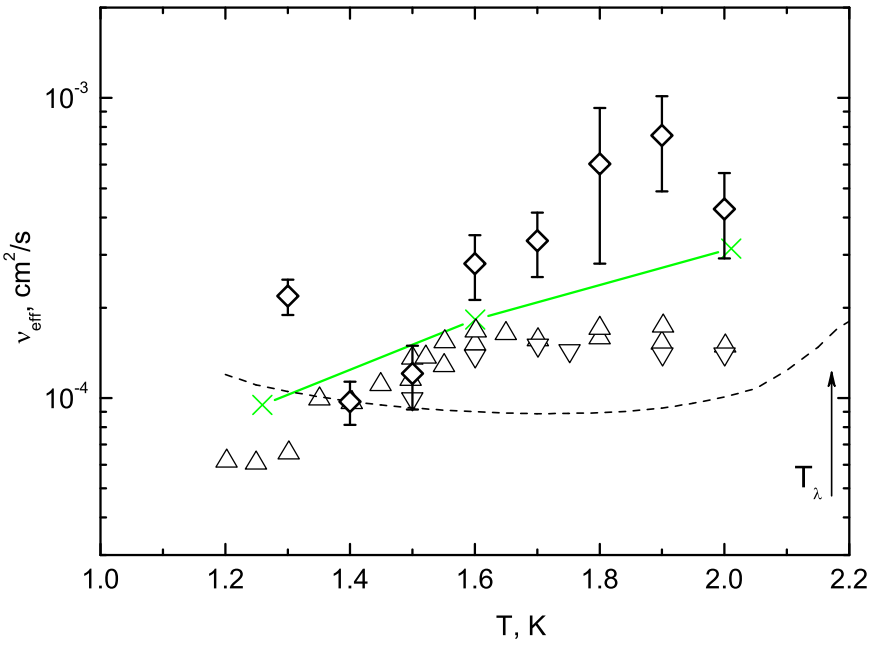

Fig. 5.1: The temperature dependence of the effective kinematic viscosity of turbulent He II. The open diamond with error bars represent the mean value over our new data from both channels ateach temperature. Up- and down-triangles are corrected data from Fig. 2 of [51] (for more ditale see [P6]), deduced from the decaying vortex line density in the Oregon experiments with unconventional (up-triangles) and conventional (down-triangles) grids. The crosses connected by the solid line represent a model calculation for $\nu_{eff}(T)$ [45]. The dotted line is a plot of kinematic viscosity of He II based on the total fluid density [28].

It is useful at this stage to write few comments on the Oregon experiments. The original second sound Oregon data on decaying He II turbulence [43, 19, 18, 47, 11] have been obtained using a grid of a rather unconventional design in that the 65% open grid consisted of only four parallel rectangular tines crossed by a single tine at 45 degrees, to which a centered pull rod was attached. This might have caused a difference in the nature of turbulence generated by such a grid with respect to turbulence generated by a grid of conventionally accepted geometry. Therefore Niemela and coworkers [51] later repeated measurements of decaying vortex line density in the same 1×1 cm^2 channel using a newly designed grid consisting of 28 rectangular tines of width 0.012 cm forming 13×13 full meshes across the channel of approximate dimension $M = 0.064$ cm. That the decay data indeed follow the -3/2 power law very closely is further strengthened by an additional analysis, see Fig. 9 in Ref. [48]. Values of $\nu_{eff}(T)$ deduced from the decay data originating from relatively high mesh Reynolds number turbulence $Re_M = v_g M \rho / \mu$

of order 10^5, where v_g is the grid velocity, M is the mesh size, ρ is the total density of He II and μ its dynamic viscosity, do not differ dramatically from the data obtained with the original unconventional grid, although they systematically lie about 10% lower (see Fig. 5.1).

The towed grid and counterflow generated data series are consistent with each other, the counterflow data displaying larger scatter. The displayed error bars reflect only the statistical scatter or the data, which is mostly caused by the fact that for generating counterflow turbulence a large heat input up to 1 W has to be applied to the dead end of the channel and then abruptly switched off. Although in the experiment the total heat input to the cryostat is kept constant (the power is not switched off but to another matching heater placed outside the channel in the helium bath), it is very difficult to stabilize the bath temperature, even with an additional bath heater and a temperature controller in use. Minimizing temperature fluctuations that necessarily follow switching off the channel heater is an experimental challenge. Fine tuning of the electronics at any particular temperature is needed before reproducible decay curves closely following the -3/2 power law (such as shown in Fig. 4.12 and in [35, 22] and [P3]) can be measured. This becomes increasingly difficult both at the lowest and highest displayed temperatures and hardly possible above 2 K, where second sound velocity steeply depends on temperature and therefore temperature fluctuations affect the propagation of second sound in the channel more strongly. Another source of a systematic error might be coupling between transverse and longitudinal second sound modes in the channel, which could lead to slightly distorted values of linewidth Δ_0 entering Eq. 4.6.

Within experimental error, calculated values of $\nu_{eff}(T)$ for two square channels do not depend on the channel size, in accord with Eq. 4.10. It is clear that the effective kinematic viscosity of *turbulent* He II $\nu_{eff}(T)$ distinctly differs from the tabulated values of kinematic viscosity of He II [28] defined as the dynamic viscosity over the total density, $\nu = \mu/\rho$ (see the dotted line in Fig. 5.1). A model calculation [45] based on the assumption that the effective kinematic viscosity is entirely due to mutual friction is also included in Fig. 5.1.

To conclude this part of the Discussion chapter on the decaying counterflow, we present experimental values of effective kinematic viscosity of turbulent He II, over the temperature range where the temporal decays of thermal counterflow and towed grid turbulence have been investigated using the second sound attenuation technique. It is truly remarkable that, although the steady-states of the grid-generated turbulence in He II and the thermally induced counterflow He II turbulence are very different in character [45], their late decays display the universal classical power law of the form of Eq. 4.10, moreover,

the deduced values of effective kinematic viscosity are consistent with each other as well as with the model calculation [45].

5.2 Discussion on pure superflow experiments

In the previous Chapter we described rather unexpected experimental results obtained in our experimental study of He II flow restricted to pure net superflow through channels with ends blocked by superleaks. In particular, two different, physically distinct turbulent states A and B have been observed for the first time and we have a formidable task of introducing suitable phenomenological model that would capture the observed flow phenomena and explain the underlying physics.

5.2.1 Steady-state pure superflow – first critical velocity

As we have described in the previous Chapter, upon increasing the heat power from zero we observe no quantized vortices in the channel until the first critical velocity v_{cr}^I is reached. This statement is an oversimplification that needs additional explanation, for the following reasons. It is well known that any macroscopic size sample of He II always contains remnant vortices and there have been even attempts to estimate their vortex line density depending on the geometry of the cell which contains a stationary sample of He II [52]. One particular reason is that any wall in contact with He II can be considered as rough on the length scale of the size of vortex core - the healing length $\xi \simeq 10^{-10}$ m. Excrescences on the wall then serve as suitable pinning sites for these remnant vortices; in our case the porous membranes used to make the second sound transducer and receiver ought to act as rather efficient pinning area for such remnant vortices. They may stretch across the channel, or exist in form of small vortex loops. Their density and configuration depend on the history of the sample and this is why our undisturbed second sound amplitude a_0 measured at resonance without any thermally induced flow through the channel is not exactly reproducible - the accuracy is typically slightly better than 1 per cent.

Neglecting the remnant vorticity, until the first critical velocity v_{cr}^I is reached the flow of the superfluid component is potential (or we can define it as largely potential) and the normal component stays quiescent.

Let us compare our observations with those of previous investigators. As far as we know, the first experiments on pure superflow have been performed by Tough's group

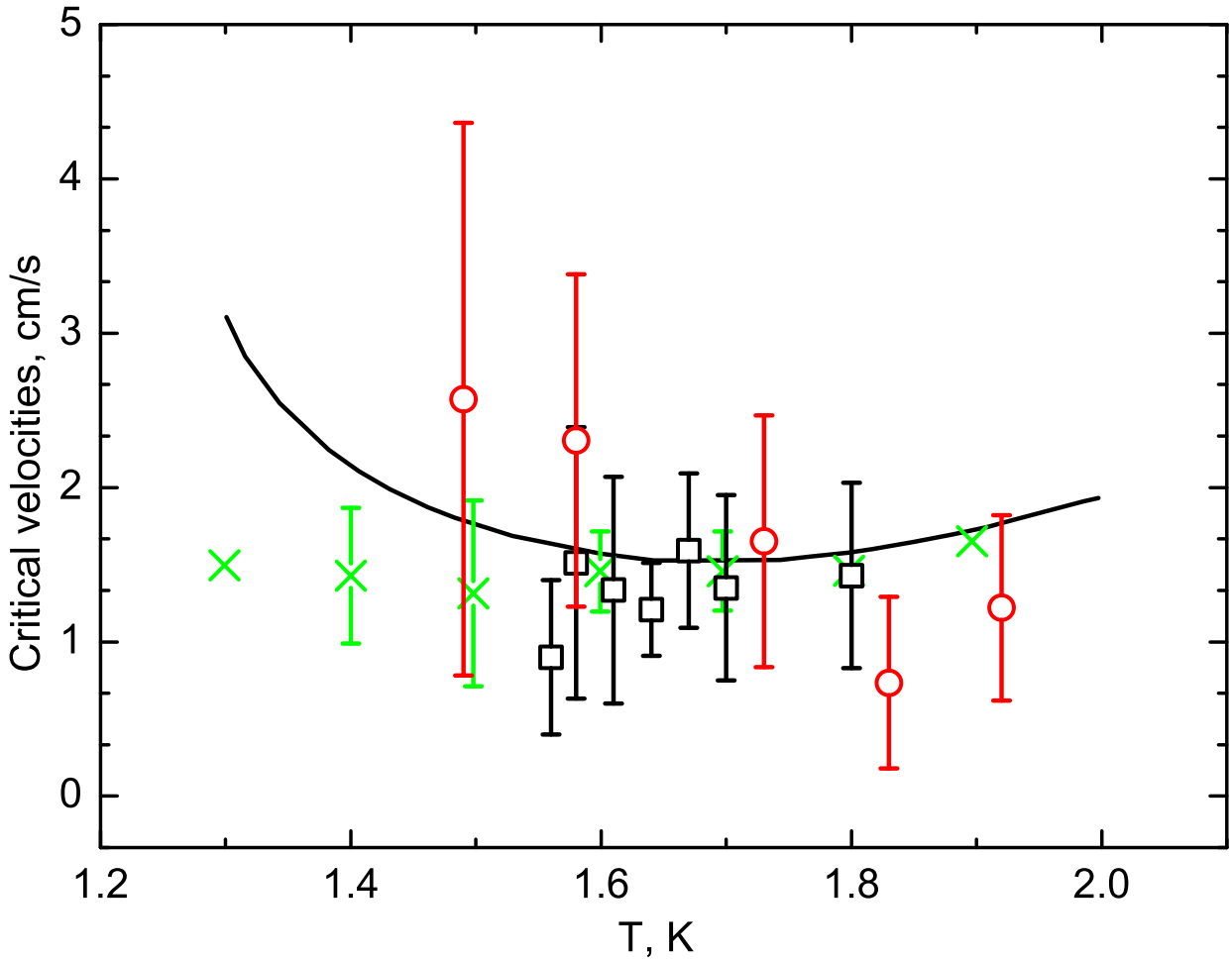

Fig. 5.2: The critical velocities v_{cr}^{I} as observed in both channels (open red circles – 6 mm channel, open black squares – 10 mm channel) plotted versus temperature. Green crosses (experiment) and solid black line (prediction of the Schwarz theory) are taken from the work of Baehr and Tough.

[23], both in circular ($id = 0.13$ mm) and rectangular (0.057×0.57 mm^2) cross-section. These first experiments, however, gave no evidence of any critical velocity. However, in later careful experiments of this group with a circular ($id = 0.13$ mm) tube a finite and nearly temperature independent critical velocity $v_{\rm cr}^{\rm I}$ was found, of about 1.5 cm/s [33] (see Fig. 2.6). The authors assumed that (as it takes place in thermal counterflow [21]) $v_{\rm cr}^{\rm I}$ scales with the size of the channel, d, and in Ref. [33] the results are given in the dimensionless form of a "superfluid Reynolds number"

$$Re_{\rm s} = \frac{v_{\rm cr}^{\rm I} d}{\kappa}, \tag{5.1}$$

where κ denotes the circulation quantum.

Fig. 5.2 displays the direct comparison of their observed critical velocity $v_{\rm cr}^{\rm I}$ with our data. Our observations of $v_{\rm cr}^{\rm I}$ in two channels of sizes 6 and 10 mm, within the error bars, agree with each other as well as with the observed critical velocity $v_{\rm cr}^{\rm I}$ of Ref. [33]. This agreement is rather surprising, as our channels are almost two orders of magnitude wider than the channel used in the work of Baehr and Tough.

We are therefore forced to conclude that the "superfluid Reynolds number" scaling does not hold. On the contrary, the agreement of our data with those obtained in a channel two orders of magnitude thinner strongly suggests that the observed critical velocity $v_{\rm cr}^{\rm I}$ is an intrinsic property of a self-sustaining tangle, in accord with the early considerations and calculations of Schwarz [46] for steady homogeneous counterflow which do not take explicitly into account any influence of the channel walls and predict the weakly temperature dependent v_{cr}^{I} of about 1 cm/s. This conclusion ought to be valid for pure superflow, as well as, via Galilean transformation also for *homogeneous* thermal counterflow.

5.2.2 Steady-state pure superflow – A-state

Above the critical velocity $v_{\rm cr}^{\rm I}$ the turbulent A-state occurs in both channels, characterized by the observed vortex line density

$$L^{1/2} = \gamma(T)(v - v_{\rm cr}^{\rm I}). \tag{5.2}$$

This functional dependence is similar to that presented by Tough's group [23], based on experiments in a circular channel of inner diameter 0.13 mm, however, with much smaller $v_{\rm cr}^{\rm I}$ – we have already mentioned that these experiments gave no evidence of finite $v_{\rm cr}^{\rm I}$. Later experiments of Baehr and Tough gave, on one hand, a clear evidence of finite $v_{\rm cr}^{\rm I}$ of order 1 cm/s, on the other hand these data have not been taken up to sufficiently high superfluid velocities to extract functional dependence $L(v_s)$ above $v_{\rm cr}^{\rm I}$. Moreover, we have to stress that the measured quantity in these experiments was the temperature difference along the channel and the vortex line density was deduced from these measurements in analogy with thermal counterflow experiments assuming full isotropy and homogeneity. The direct quantitative comparison with our data is therefore not possible.

Still, the functional dependence Eq. 5.2 allows to conclude that the A-state is most likely analogical to thermal counterflow. This is further supported by the fact that the late decay of the A-state as well as the late decay of thermal counterflow display the classical universal decay regime for decaying vortex line density, characterized by the power law with exponent -3/2. These data (such as shown in Fig. 4.11) do not span sufficiently large

range of the decaying vortex line density for precise deduction of effective kinematic viscosity, but they still allow to estimate it to be of order 5×10^{-4} cm^2/s, which is consistent with the data given in Fig. 5.1.

5.2.3 Steady-state pure superflow – B-state

We have already described that in both our channels the steady A-state, characterized by $L^{1/2} = \gamma(T)(v - v_{\rm cr}^{\rm I})$, gradually changes character and, especially in the smaller 6 mm channel can be described by

$$L = \beta(T)(v - v_{\rm cr}^{\rm II}), \tag{5.3}$$

where $v_{\rm cr}^{\rm II}$ of order few cm/s decreases with increasing temperature (see Fig. 5.2 and β only very weakly (if at all) temperature dependent (see Fig. 4.6).

Because the B-state has been experimentally observed for the first time, it poses a challenging problem of proposing plausible physical model that would capture the underlying physics. Based on our experimental data, we are offering here the following phenomenological model (see [P7]).

Our current understanding of the nature of this new B-state is stimulated by the ability of superfluid to mimic classical flows. The simplest example is the rotating bucket of He II, where the superfluid mimics solid body rotation via a hexagonal lattice of rectilinear quantized vortices, so that on length scales larger than intervortex distance the flow appears classical. Could superfluid mimic a classical laminar pipe flow?

To answer this question, let us first consider an ordinary viscous liquid which flows through a cylindrical pipe of radius R. For not very large Reynolds number the flow has a parabolic Poiseuille velocity profile which is symmetric relative to the axis of the pipe, with maximum velocity on it. In cylindrical coordinates (r, ϕ, z) with the z-axis placed on the axis of the pipe the parabolic velocity profile can be expressed as

$$\vec{v} = (0, 0, av_0(1 - \frac{r^2}{R^2})), \tag{5.4}$$

where a can be found by integration:

$$v_0 = \frac{1}{\pi R^2}\int_0^R\int_0^{2\pi} r\ dr\ d\varphi\ av_0(1 - \frac{r^2}{R^2})\ , \tag{5.5}$$

which gives $a = 2$. We shall be interested in vorticity, which in cylindrical coordinates becomes $curl\ \vec{v} = (0, 4v_0\frac{r}{R^2}, 0)$, thus its average value yields:

$$\langle\omega\rangle = \langle curl\ \vec{v}\rangle = \frac{1}{\pi R^2}\int_0^R\int_0^{2\pi} r\ dr\ d\varphi\ 4v_0\frac{r}{R^2} = \frac{8}{3}\frac{v_0}{R}\ . \tag{5.6}$$

We see that the average vorticity in the pipe is a linear function of the mean velocity; a fact which we use in building up our model, in the following way. Let us consider the situation when pure superfluid flows through such a cylindrical pipe and mimics the normal fluid behaviour with parabolic flow profile. One can imagine vortex rings of various radii located in parallel planes perpendicular to the velocity vector. Assuming that the superfluid mimics such a classical flow, we require

$$\langle \vec{\omega} \rangle = \langle curl \vec{v} \rangle = \kappa L \, , \tag{5.7}$$

in analogy with the rotation bucket. The required numerical value of vortex line density for velocity $v_0 = 10$ cm/s and channel of radius $R = 0.3$ cm (thus similar in size to our 6 mm channel) becomes $L = 8.9 \times 10^4$ cm^2/s. In other words, this would mean that the proportionality constant, the β coefficient, is $\beta \simeq 9 \times 10^3$ s cm^{-3}; only a factor of 2–3 lower than that experimentally observed. In view of simplicity of this physical picture, this seems as a remarkable coincidence. We see the semi-quantitative agreement with our observations and, probably more importantly, the correct prediction of the observed **temperature independent** linear behavior of vortex line density with mean superfluid velocity Eq. 4.8, where the second critical velociy $v_{\rm cr}^{\rm II}$ playing a role of the slip velocity on the solid boundary of the channel.

Let us add few remarks here. In our calculation we have considered a cylindrical channel with the parabolic flow profile. In fact, our experimental channels are of square cross-section, so the profile of the flow is more complicated. But more accurate calculations of β based on classical flow profile in a square pipe does not seem practical, e.g., due to insufficient entry length to expect the fully developed flow profile. It is well known that as a rule in classical fluid dynamics, in order to create the fully developed flow profile, ratio of the channel width to its length have to be 1:50. Moreover, if vortex lines are fully or partially polarized, it increases the minimum calculated value of L. So far in our considerations we ignored the normal fluid. The net normal fluid flow rate which penetrates to the channel must be zero, because the ends of the channel are blocked by superleaks. So we can exclude any kind of flow in which superfluid and normal fluid velocity fields are fully matched, such as is the case of the rotating bucket. On the other hand, the presence of vortex tangle gives rise to the mutual friction force which may induce an internal viscous flow (thus subject to no slip boundary conditions). The dissipation of energy by the mutual friction force would be minimized if suitable steady flow of the normal fluid becomes generated. Now, let us assume that deep enough in the B-state the superfluid has approximately parabolic flow profile, (which might become slightly distorted by this

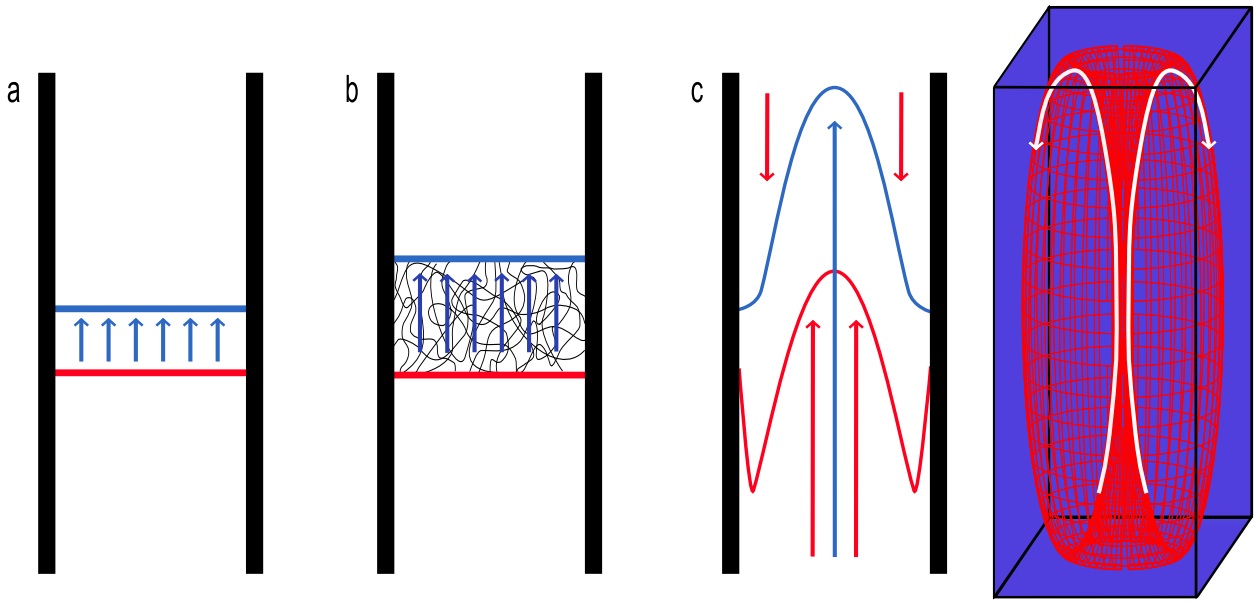

Fig. 5.3: Phenomenological model of the flow. For details, see text.

induced internal normal fluid flow). Taking into account the symmetry of the channel, it is reasonable to assume the normal flow of approximately toroidal form.

Fig. 5.3 shows the evolution of the normal and superfluid flow profiles graphically. On increasing v_s from zero, there are no quantized vortices (except remnant ones) in the channel and second sound amplitude remains unchangeable. The superfluid profile is flat (see (a) in Fig. 5.3), the normal component stays quiescent. The flow is presumably laminar, until the first critical velocity v_{cr}^I is reached. Then the A-state region, characterized by Eq. 4.7, is observed. The likely forms of normal fluid and (averaged over a distance greater than the intervortex distance) superfluid flow profiles slightly above v_{cr}^I are schematically shown in (b). The normal fluid is still approximately quiescent and the superfluid flow profile is approximately flat. In the B-state (see (c) in Fig. 5.3) the superfluid has approximately parabolic flow profile, while the normal flow is of approximately toroidal form. Could such a flow of the normal fluid be detected? We believe that the answer to this question lies in our decay data – discussion of those follows.

5.2.4 Decay of steady-state pure superflow

The key point here is the exponential part of the decay of the vortex line density that takes place after the first complex part of the decay, as it has been described in detail in previous Chapter. This exponential decay could be considered in analogy with the decay of the oscillatory motion at some particular wave number in viscous fluids (such

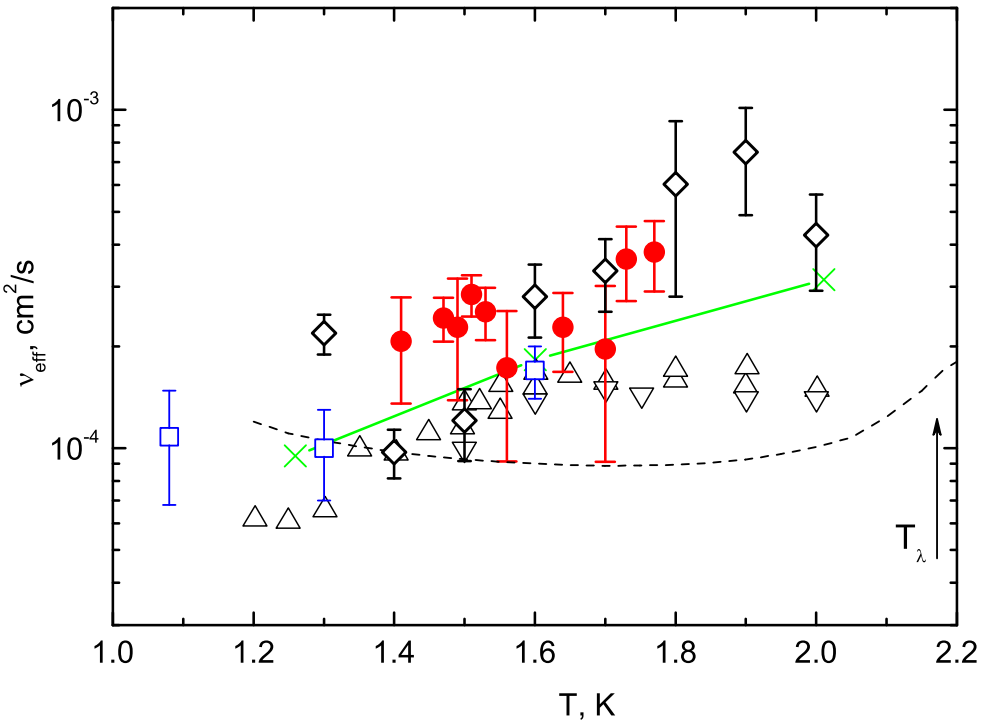

Fig. 5.4: The value of effective kinematic viscosity required by our decay model (filled red circles) together with $\nu_{eff}(T)$ deduced from decaying counterflow (open diamond), towed grid (up- and down-triangles) and spin-down experiments (blue squares) in He II (see [8], as well as with theoretical estimate (green crosses connected with the solid line)

as, e.g., decay of the gravity waves on the surface of classical fluids or viscous decay of the rotational motion of fluid inside a long cylindrical vessel) characterized by exponential decay of energy of the form

$$E = E_0 \exp\left(-\frac{t}{\tau}\right), \tag{5.8}$$

with the decay time $\tau^{-1} = 2\pi k^2$, where k is the characteristic wave number [3]. The observed τ corresponds to a quasi-viscous decay of a toroidal eddy (schematically shown in Fig. 5.3 (c)(left)): $D/2 = 2\pi/k$. It follows that the observed τ would require an effective kinematic viscosity

$$\nu_{eff} = D^2/(32\pi^2\tau) \tag{5.9}$$

That our simple model is reasonable is evident from comparison with the theoretical calculation of ν_{eff} (see Chapter 2.5.3) as well as with available data deduced from other experiments. These include (i) the Prague decaying thermal counterflow, (ii) the Oregon decaying towed grid He II turbulence (both using the second sound attenuation as the detection technique) and (iii) and the Manchester spin-down experiments (ion detection

technique). Fig. 5.4 shows all these data together.

Formula 5.9 would predict that in the 10 mm channel, τ ought to be about twice as large, as $\tau \sim D^2$. We have no systematic data from the bigger channel (for experimental reasons explained above), but our data allow to conclude that this prediction is fulfilled qualitatively.

Chapter 6

Conclusions

The present Thesis is dedicated to experimental studies of both steady-state and decaying flows and quantum turbulence in superfluid ^{4}He, which was generated thermally, by applying heat power either to the dead end of the counterflow channel or to the fountain pump above the channel with ends blocked by sintered silver superleaks. Additionally, the Thesis contains results and analysis of experiments on decaying thermal counterflow. The main results can be characterized as follows:

(i) An experimental apparatus for generation and detection of quantum turbulence in He II has been design and constructed, allowing generation and detection of an upward superflow, induced by the fountain pump through vertical channels of square cross-section with ends blocked by sintered silver superleaks. Home made lifting system based on a capacitive level meter, ac capacitance bridge, PC controlled Maxon DC stepper motor and the developed software based on the multifunctional graphical NI LabView pack allows open helium bath experiments with continuous control of the helium level. Various types of tests confirmed that this apparatus is capable of measurements of the steady-state as well as decaying vortex line density in such flows, using the second sound attenuation technique to probe them. The construction of second sound transducers and receivers based on gold-evaporated porous Nuclepore membranes has been largely improved during this work, leading to better sensitivity and reproducibility of this remarkable detection technique.

(ii) Steady-state flows of He II in two channels of different square cross-section restricted to pure net superflow have been experimentally investigated within the temperature range 1.45-1.95 K. On increasing the heat power, $\dot{Q}$, several physically distinct flows have been found. The first one is a potential vortex-free superflow, which upon reaching the first critical velocity gives way to the turbulent A-state, where approximately homo-

geneous and isotropic self-sustaining vortex tangle exists, similar as in thermal counterflow. An important experimental fact is that the first critical velocity v_{cr}^{I}, of order 1 cm/s, does not depend on the channel size and is therefore an intrinsic property of the self-sustaining vortex tangle. The turbulent A-state, characterized by the vortex line density $L^{1/2} = \gamma(T)(v_s - v_{cr}^{I})$ gradually changes into the newly discovered B-state, characterized by $L = \beta(v_s - v_{cr}^{II})$, where β seems temperature independent.

(iii) The temporal decay of steady-state B generated for various superfluid velocities has been investigated. When $\dot{Q}$ is switched off, after a complicated fast initial part of the decay that probably involves thermal relaxation and partial depolarization of the vortex tangle, the decay gradually becomes exponential in character, of the form $L \propto exp{-t/\tau}$, where the characteristic decay time τ is only weakly temperature dependent.

(iv) We have developed a simple phenomenological model qualitatively capturing all the experimentally observed features. The model is built on the assumption that in the B-state the superfluid velocity profile tries to match the classical laminar parabolic flow profile. Due to the mutual friction force, a confined viscous normal fluid flow is induced inside the channel. When the fountain pump is switched off, after an initial decay a coupled confined quasi-laminar flow of toroidal form of both components establishes, giving rise to the observed exponential decay.

(v) Based on our analysis of experimental results on decaying counterflow in two channels of square cross-section, we have deduced the temperature dependence of the effective kinematic viscosity of turbulent He II, $\nu_{eff}(T)$. It is shown to agree qualitatively with the published data for $\nu_{eff}(T)$ calculated based on experiments on decaying grid-generated He II turbulence.

(vi) Additionally, we have used the developed phenomenological model for deducing $\nu_{eff}(T)$ from our second sound data on decaying pure superflow. With no fitting parameters, the values of $\nu_{eff}(T)$ deduced from the exponential part of the decay agree quantitatively with those calculated based on various other experiments (decaying towed grid He II turbulence, spin down experiments, decaying counterflow) as well as with the theoretical model introduced by Vinen and Niemela. This fact gives us confidence that our phenomenological model is physically sound.

Bibliography

[1] P. L. Kapitza, *Collected scientific papers. Low-temperature physics and technology*. Moscow: Nauka, 1989.

[2] D. R. Tilley and J. Tilley, *Superfluidity and Supercondactivity*. Adam Hilger Ltd., 2 ed., 1986.

[3] L. D. Landau and E. M. Lifshitz, *Hydrodynamics*. M.: Nauka, 3 ed., 1986.

[4] H. E. Hall and W. F. Vinen, "Experiments on the propagation of second sound in uniformly rotating helium II," *Proceedings of the Royal Society of London*, vol. 238, p. 204, 1957.

[5] H. E. Hall and W. F. Vinen, "The theory of mutual friction in uniformly rotating helium II," *Proceedings of the Royal Society of London*, vol. 238, p. 215, 1957.

[6] W. F. Vinen, "Detection of single quanta of circulation in liquid helium II," *Proceedings of the Royal Society of London*, vol. 260, p. 218, 1961.

[7] G. P. Bewley, D. P. Lathrop, and K. R. Sreenivasan, "Superfluid helium - visualization of quantized vortices," *Nature*, vol. 441, p. 588, 2006.

[8] P. M. Walmsley, A. I. Golov, H. E. Hall, A. A. Levchenko, and W. F. Vinen, "Dissipation of quantum turbulence in the zero temperature limit," *Physical Review Letters*, vol. 99, p. 265302, 2007.

[9] E. J. Yarmchuk and R. E. Packard, "Photographic study of quantized vortex line," *Journal of Low Temperature Physics*, vol. 46, p. 478, 1982.

[10] I. M. Khalatnikov, *Introduction to the Theory of Superfluidity*. Benjamine, New York, 1965.

[11] S. R. Stalp. PhD thesis, University of Oregon, Eugene, U.S.A., 1998.

[12] H. A. Snyder and Z. Putney, "Angular dependence of mutual friction in rotating He II," *Physical Review*, vol. 150, p. 110, 1966.

[13] P. Mathieu, B. Placais, and Y. Simon, "Spatial distribution of vortices and anisotropy of mutual friction in rotating He II," *Physical Review B*, vol. 29, p. 2489, 1984.

[14] R. P. Feynman, "Application of quantum mechanics to liquid helium.," *Progress in Low Temperature Physics*, vol. 1, p. 17, 1955.

[15] A. P. Finne, T. Araki, R. Blaauwgeers, V. B. Eltsov, N. B. Kopnin, M. Krusius, L. Skrbek, M. Tsubota, and G. E. Volovik, "An intrinsic velocity-independent criterion for superfluid turbulence," *Nature*, vol. 424, p. 1022, 2003.

[16] A. M. Guenault, V. Keith, C. J. Kennedy, S. G. Mussett, and G. R. Pickett, "The mechanical behavior of a vibrating wire in superfluid ^{3}He-B in the ballistic limit," *Journal of Low Temperature Physics*, vol. 62, p. 511, 1986.

[17] M. Blazkova, M. Clovecko, E. Gazo, L. Skrbek, and P. Skyba, "Experimental setup for generation andprobing He II flows," *Journal of Low Temperature Physics*, vol. 148, p. 305, 2007.

[18] L. Skrbek, J. J. Niemela, and R. J. Donnelly, "Four regimes of decaying grid turbulence in a finite channel," *Physical Review Letters*, vol. 85, p. 2973, 2000.

[19] S. R. Stalp, L. Skrbek, and R. J. Donnelly, "Decay of grid turbulence in a finite channel," *Physical Review Letters*, vol. 82, p. 4831, 1999.

[20] W. F. Vinen, "Experiments on steady heat currents," *Proceedings of the Royal Society of London*, vol. 240, p. 114, 1957.

[21] J. T. Tough, "Superfluid turbulence," *Progr. in Low Temp. Phys.*, vol. VIII, 1982.

[22] L. Skrbek, A. V. Gordeev, and F. Soukup, "Decay of counterflow He II turbulence in a finite channel: Possibility of missing links between classical and quantum turbulence," *Physical Review E*, vol. 67, p. 047302, 2003.

[23] R. A. Ashton, L. B. Opatowsky, and J. T. Tough, "Turbulence in pure superflow," *Physical Review Letters*, vol. 46, p. 658, 1981.

[24] J. T. Tough, R. A. Ashton, and L. B. Opatovsky, "Superfluid turbulence in counterflow and pure superflow," *Physica B and C*, vol. 108, 1981.

[25] L. B. Opatowsky and J. T. Tough, "Homogeneity of turbulence in pure superflow," *Physical Review B*, vol. 24, p. 5420, 1981.

[26] W. F. Vinen, "Experiments on transient effect," *Proceedings of the Royal Society of London*, vol. 240, p. 128, 1957.

[27] K. W. Schwarz, "Three-dimensional vortex dynamics in ^{4}He: Homogeneous superfluid turbulence," *Physical Review B*, vol. 38, p. 2398, 1988.

[28] R. J. Donnelly and C. F. Barenghi, "The observed properties of liquid helium at the saturated vapor pressure," *Journal of Phys. and Chem. Ref. Data*, vol. 27, p. 1217, 1998.

[29] K. W. Schwarz and J. R. Rozen, "Anomalous decay of turbulence in superfluid ^{4}He," *Physical Review Letters*, vol. 66, p. 1898, 1991.

[30] K. W. Schwarz and J. R. Rozen, "Transient behavior of supefluid turbulence in a large channel," *Physical Review B*, vol. 44, p. 7565, 1991.

[31] F. P.Milliken, K. Schwarz, and C. Smith, "Free decay of superfluid turbulence," *Physical Review Letters*, vol. 48, p. 1204, 1982.

[32] J. T. Tough, R. A. Ashton, and L. B. Opatowsky, "Superfluid turbulence in counterflow and pure superflow," *Physica B*, vol. 108, p. 1127, 1981.

[33] M. L. Baehr, L. B. Opatowsky, and J. T. Tough, "Transition from dissipationless superflow to homogeneous superfluid turbulence," *Physical Review Letters*, vol. 51, p. 2295, 1983.

[34] C. F. Barenghi, A. V. Gordeev, and L. Skrbek, "Depolarization of decaying counterflow turbulence in He II," *Physical Review E*, vol. 74, p. 026309, 2006.

[35] C. F. Barenghi and L. Skrbek, "On decaying counterflow turbulence in He II," *Journal of Low Temperature Physics*, vol. 146, p. 5, 2007.

[36] G. K. Batchelor, *Homogeneous Turbulence*. Cambridge: Cambridge University Press, 1953.

[37] U. Frisch, *Turbulence*. Cambridge: Cambridge University Press, 1995.

[38] L. Skrbek and S. R. Stalp, "On the decay of homogeneous isotropic turbulence," *Physics of Fluids*, vol. 12, p. 1997, 2000.

[39] I. P. D. D. Silva and H. J. S. Fernando, "Oscillating grids as a source of nearly isotropic turbulence," *Physics of Fluids*, vol. 6, no. 7, p. 2455, 1994.

[40] H. Touil, J. P. Bertoglio, and L. Shao, "The decay of turbulence in a bounded domain," *Journal of Turbulence*, vol. 3, no. 049, 2002.

[41] J. Maurer and P. Tabeling, "Local investigation of superfluid turbulence," *Europhysics Letters*, vol. 43, p. 29, 1998.

[42] K. R. Sreenivasan, "On the universality of the kolmogorov constant," *Physics of Fluids*, vol. 7, p. 2778, 1995.

[43] M. R. Smith, R. J. Donnely, N. Goldenfeld, and W. Vinen, "Decay of vorticity in homogeneous turbulence," *Physical Review Letters*, vol. 71, p. 2583, 1993.

[44] W. F. Vinen, "Classical character of turbulence in a quantum liquid," *Physical Review B*, vol. 61, p. 1410, 2000.

[45] W. F. Vinen and J. J. Niemela, "Quantum turbulence," *Journal of Low Temperature Physics*, vol. 128, p. 167, 2002.

[46] K. W. Schwarz, "Turbulence in superfluid helium: Steady homogeneous counterflow," *Physical Review B*, vol. 18, p. 245, 1978.

[47] S. Stalp, J. J. Niemela, W. F. Vinen, and R. J. Donnelly, "Dissipation of grid turbulence in He II," *Physics of Fluids*, vol. 14, p. 1377, 2002.

[48] J. J. Niemela and K. R. Sreenivasan, "The use of cryogenic helium for classical turbulence: promises and hurdles," *Journal of Low Temp. Phys.*, vol. 143, p. 163, 2006.

[49] V. F. Mitin, "Miniature resistance thermometers based on Ge films on GaAs," *Advances in Cryogenic Engineering*, vol. 43, 1982.

[50] A. V. Gordeev, F. Soukup, and L. Skrbek, "Decay of counterflow turbulence in He II," in *20 General conference, Condensed matter division*, (Prague), 2004.

[51] J. J. Niemela, K. R. Sreenivasan, and R. J. Donnelly, "Grid generated turbulence in helium II," *Journal of Low Temperature Physics*, vol. 138, p. 537, 2005.

[52] D. D. Awschalom and K. W. Schwarz, "Observation of a remanent vortex-line density in superfluid helium," *Physical Review Letters*, vol. 52, no. 1, p. 49, 1984.

List of Publications

This Thesis is a monograph, which contains some unpublished material, but is mainly based on the following publications.

[P1] T. V. Chagovets, M. Rotter, L. Skrbek "Second sound – probe for investigation of stability of He II flow" *in WDS'04 Proceeding of contributed papers: Part III – Physics* ed. by J. Safrankova, Prague, Matfyzpress, 2004, pp. 465-468.

[P2] T. V. Chagovets, M. Rotter, J. Sindelar, F. Soukup and L. Skrbek "Turbulence in He II generated by superflow" *LT24 AIP Conference Proceedings 850*, ISBN 0-7354-0347-3, 2006, pp. 209-210.

[P3] A. V. Gordeev, T. V. Chagovets, F. Soukup and L. Skrbek "Decaying counterflow turbulence in He II" *Journal of Low Temperature Physics*, vol. 138, 2005, pp. 549-554.

[P4] T. V. Chagovets, L. Dolezal, J. Dupak, A. V. Gordeev, J. Pracharova, M. Rotter, F. Soukup, J. Sindelar and L. Skrbek "Experimental setup for generating and probing He II flows" *Acta Physica Slovaca*, vol. 56, 2006, pp. 173-176.

[P5] T. V. Chagovets, A. V. Gordeev, M. Rotter, F. Soukup, J. Sindelar and L. Skrbek "Steady and decaying quantum turbulence generated in He II flow channel by counterflow and superflow" *Acta Physica Slovaca*, vol. 56, 2006, pp. 169-172.

[P6] T. V. Chagovets, A. V. Gordeev, L. Skrbek "Effective kinematic viscosity of turbulent He II" *Physical Review E*, vol. 76, 2007, pp. 027301-4.

[P7] T. V. Chagovets, L. Skrbek "Steady and decaying flow of He II in a channel with ends blocked by superleaks" *submitted to Phys. Rev. Letters*.

Other publications

- M. Blazkova, T. V. Chagovets, M. Rotter, D. Schmoranzer, L. Skrbek "Cavitation in liquid helium observed in a flow due to a vibrating quartz fork" *Journal of Low Temperature Physics*, vol. 150, 2008, pp. 194-199.

- A. G. Kuchin, A. M. Gurevich, V. M. Dmitriev, A. V. Terekhov, T. V. Chagovets, A. S. Ermolenko "Magnetism of the singlet-singlet system PrNi5-xCUx" *Journal of Alloys and Compounds*, vol. 368, 2004, pp. 75-78.

- V. N. Eropkin, T. V. Chagovets "Setup for calorimetric measurements at temperatures below 1 K" *Low Temperature Physics*, vol. 29, 2003, pp. 957-959.

- A. G. Anders, N. N. Efimova, V. B. Valiev, S. R. Kufterina, A. M. Gurevich, A. I. Krivchikov, A. V. Terekhov, T. V. Chagovets " Low-temperature specific heat of frustrated ferrimagnets BaFe12-xInxO19 with x=3.0 and x=3.6" *Low Temperature Physics*, vol. 29, 2003, pp. 305-309.

- R. de Graaf, R. E. Solntsev, T. V. Chagovets, V. B. Eltsov, R. Hanninen and M. Krusius "The dynamics of vortex generation in superfluid 3He-B" *preprint arXiv:0708.3003v1*, 2007.

- M. Blazkova, T. V. Chagovets, J. Pesicka, M. Rotter and L. Skrbek "Quartz Tuning Fork - Frequency Standard For Digital Watches - an Efficient Tool To Study Boundary Layer Flows" *in Proceeding of the colloquium fluid dynamics*, ed. by P. Jonas, V. Uruba, Prague, Institute of Thermodynamics, October 25-27, 2006, pp. 9-12.

- M. Blažková, T. V. Chagovets, M. Rotter, D. Schmoranzer and L. Skrbek "Technika PIV pro studium proudění kryogenního helia" *in Proceeding of 21st symposium on anemometry*, ed. by Z. Chăra a L. Klaboch, Holany-Litice, May 29-30, 2007, pp. 29-30.

List of Citations

- E. Kozik, B. Svistunov "Scanning superfluid-turbulence cascade by its low-temperature cutoff" *Physical Review Letters*, vol. 100, 2008, pp. 195302.
- C. F. Barenghi, Y. A. Sergeev, N. Suramlishvili "Ballistic propagation of thermal excitations near a vortex in superfluid He-3-B" *Physical Review B*, vol. 77, 2008, pp. 104512.
- P. M. Walmsley, A. I. Golov, H. E. Hall, A. A. Levchenko, W. F. Vinen "Dissipation of quantum turbulence in the zero temperature limit" *Physical Review Letters*, vol. 99, 2007, pp. 265302.
- C. F. Barenghi, L. Skrbek "On decaying counterflow turbulence in He II" *Journal of Low Temperature Physics*, vol. 149, 2007, pp. 05.
- J. J. Niemela, K. R. Sreenivasan "The use of cryogenic helium for classical turbulence: Promises and hurdles" *Journal of Low Temperature Physics*, vol. 143, 2006, pp. 163.
- C. F. Barenghi, A. V. Gordeev, L. Skrbek "Depolarization of decaying counterflow turbulence in He II" *Physical Review E*, vol. 74, 2006, pp. 026309.
- L. Skrbek "Energy spectra of quantum turbulence in He II and He-3-B: A unified view" *JETP Letters*, vol. 83, 2006, pp. 127.